Research Paper

GEOSPHERE

GEOSPHERE, v. 17, no. 3

https://doi.org/10.1130/GES02299.1

13 figures; 4 plates; 4 tables; 1 set of supplemental files and 1 individual supplemental file

CORRESPONDENCE: rwitter@usgs.gov

CITATION: Witter, R.C., Bender, A.M., Scharer, K.M., DuRoss, C.B., Haeussler, P.J., and Lease, R.O., 2021, Geomorphic expression and slip rate of the Fairweather fault, southeast Alaska, and evidence for predecessors of the 1958 rupture: Geosphere, v. 17, no. 3, p. 711–738, https://doi.org/10.1130/GES02299.1.

Science Editor: Shanaka de Silva
Guest Associate Editor: H. Gary Greene

Received 12 June 2020
Revision received 12 November 2020
Accepted 2 February 2021

Published online 6 May 2021

THEMED ISSUE: Tectonic, Sedimentary, Volcanic and Fluid Flow Processes along the Queen Charlotte–Fairweather Fault System and Surrounding Continental Margin

Geomorphic expression and slip rate of the Fairweather fault, southeast Alaska, and evidence for predecessors of the 1958 rupture

Robert C. Witter[1], Adrian M. Bender[1], Katherine M. Scharer[2], Christopher B. DuRoss[3], Peter J. Haeussler[1], and Richard O. Lease[1]

[1]U.S. Geological Survey, Alaska Science Center, 4210 University Drive, Anchorage, Alaska 99508, USA
[2]U.S. Geological Survey, Earthquake Science Center, 525 S. Wilson Street, Pasadena, California 91106, USA
[3]U.S. Geological Survey, Geologic Hazards Science Center, 1711 Illinois Street, Golden, Colorado 80401, USA

ABSTRACT

Active traces of the southern Fairweather fault were revealed by light detection and ranging (lidar) and show evidence for transpressional deformation between North America and the Yakutat block in southeast Alaska. We map the Holocene geomorphic expression of tectonic deformation along the southern 30 km of the Fairweather fault, which ruptured in the 1958 moment magnitude 7.8 earthquake. Digital maps of surficial geology, geomorphology, and active faults illustrate both strike-slip and dip-slip deformation styles within a 10°–30° double restraining bend where the southern Fairweather fault steps offshore to the Queen Charlotte fault. We measure offset landforms along the fault and calibrate legacy ^{14}C data to reassess the rate of Holocene strike-slip motion (≥49 mm/yr), which corroborates published estimates that place most of the plate boundary motion on the Fairweather fault. Our slip-rate estimates allow a component of oblique-reverse motion to be accommodated by contractional structures west of the Fairweather fault consistent with geodetic block models. Stratigraphic and structural relations in hand-dug excavations across two active fault strands provide an incomplete paleoseismic record including evidence for up to six surface ruptures in the past 5600 years, and at least two to four events in the past 810 years. The incomplete record suggests an earthquake recurrence interval of ≥270 years—much longer than intervals <100 years implied by published slip rates and expected earthquake displacements. Our paleoseismic observations and map of active traces of the southern Fairweather fault illustrate the complexity of transpressional deformation and seismic potential along one of Earth's fastest strike-slip plate boundaries.

INTRODUCTION

The fastest slipping continent-ocean strike-slip fault on Earth defines the western North American plate boundary in southeastern Alaska and western Canada—the Queen Charlotte–Fairweather fault system (Molnar and Dayem, 2010; Brothers et al., 2020). At the northern end of the fault system, the Fairweather fault accommodates most or all of the relative motion between North America and the eastern margin of the Yakutat block (Plafker et al., 1978; Elliott and Freymueller, 2020), an overthickened oceanic plateau that is colliding into southern Alaska (Bruns, 1983; Plafker et al., 1994) (Fig. 1). Satellite geodesy spanning more than a decade and geophysical block models place 35–46 mm/yr of right-lateral motion on the Fairweather fault and 5–8 mm/yr of contraction on reverse faults to the west (Elliott and Freymueller, 2020), including the Lituya Bay–Icy Point thrust fault (Plafker, 1967; MacKevett et al., 1971; Risley et al., 1992) (Fig. 2).

Between 1949 and 2013, the North American plate boundary along western Canada and southeastern Alaska ruptured in a series of large earthquakes ranging in magnitude from 7.3 to 8.1, including the 1958 moment magnitude (M_w) 7.8 Fairweather earthquake, which ruptured >260 km of the Fairweather fault from Cross Sound to Yakutat Bay (Stauder, 1960; Sykes, 1971; Page, 1973; Schell and Ruff, 1989; Doser and Lomas, 2000; Doser, 2010) (Fig. 1). Most of the onshore 1958 fault rupture is hidden beneath ice or water in extremely remote areas that lack topographic and bathymetric data of sufficient detail to accurately map active tectonic deformation. However, post-1958 earthquake surveys of surface fault ruptures measured 2.5–6.5 m of right-lateral displacement and up to ~1.1 m of vertical displacement between Lituya Bay and Icy Point (Tocher and Miller, 1959; Tocher, 1960) (Fig. 2). The landscape along this transpressive bend in the Fairweather fault records a late Quaternary history of deformation caused by right-lateral and reverse faulting. At Icy Point (Fig. 2), for example, flights of uplifted marine terraces imply persistent late Pleistocene transpressive deformation where the Fairweather fault projects offshore (Hudson et al., 1976; Plafker et al., 1978; Mann and Ugolino, 1985).

This paper focuses on the southern ~30 km of the onshore 1958 earthquake rupture, between Crillon Lake and where the Fairweather fault steps 3 km offshore and bends 10°–30° west (Fig. 2) to a simpler, linear fault trace in the seafloor (Brothers et al., 2020) (Fig. 2). Despite rapid slip (Plafker et al., 1978; Elliott and Freymueller, 2020) and recent surface fault rupture, no paleoseismic or geomorphological data sets characterized seismic hazards along this section of the Fairweather fault prior to our study.

Here, we map surficial geology and active fault traces that strike 10°–30° more westerly than the local direction (~337°) of Yakutat block motion relative

Rob Witter https://orcid.org/0000-0002-1721-254X

to North America (Brothers et al., 2020). Our interpretations of active fault traces rely on 1-m resolution, light detection and ranging (lidar)–based digital elevation models (DEMs; Plate 1), field observations documenting the effects of the 1958 earthquake (Tocher and Miller, 1959; Tocher, 1960), and our own observations during expeditions in 2016 and 2017. Our field observations verified the presence of active faults, glacial landforms, marine and fluvial terraces, and other features depicted on large-format plates and a geographic information systems database (Plates 1–4 and GIS shapefiles in Supplemental Material 1[1]). Field and lidar-measured offset landforms combined with calibrated legacy ^{14}C data permit reassessment of the Holocene Fairweather fault slip rate. We also report evidence for predecessors of the 1958 earthquake based on paleoseismic trenching 14 km southeast of Lituya Bay. The pervasive west-side-up deformation and structural complexity of the southern Fairweather fault imply high rates of right-lateral slip and dip-slip within a transpressive bend between Lituya Bay and Icy Point, where the fault trace steps offshore (Fig. 2).

REGIONAL GEOLOGIC AND SEISMOTECTONIC SETTING

The Fairweather fault strikes through Desolation Valley (Fig. 2), a regional topographic depression first recognized by Mertie (1931) as a "great fault rift." This 280-km-long, ice-scoured, linear trough visible in satellite images separates the Fairweather Range of the St. Elias Mountains from the coastal foothills along the Gulf of Alaska that locally exceed 1300 m elevation. East of the fault valley, the Fairweather Range exposes amphibolite-grade rocks of the Chugach metamorphic complex (Hudson and Plafker, 1982; Dusel-Bacon, 1994; Pavlis and Sisson, 1995); these rocks were accreted onto North America in the late Mesozoic, metamorphosed, and intruded by Paleogene plutons before the Yakutat block collided into Alaska at ca. 30 Ma (Plafker et al., 1994; Pavlis et al., 2004). West of the fault, the coastal foothills consist of Mesozoic flysch and mélange facies of the Yakutat Group, Cenozoic granitic rocks, and middle Miocene–Pleistocene siltstones and sandstones of the Topsy and Yakataga Formations (Marincovich, 1980; Rau et al., 1983). The Topsy and Yakataga Formations belong to a distinctive cover sequence that chronicles Yakutat terrane collision, accretion, and glaciation (Plafker et al., 1994; Pavlis et al., 2004).

The Fairweather fault accommodates most of the right-lateral component of transpression along the eastern boundary of the Yakutat block (Elliott and Freymueller, 2020), but geologically derived slip rates consistently exceed geodetic estimates. Le Pichon (1968) first estimated 50 mm/yr of slip across the fault by modeling the northeast Pacific seafloor spreading rates of Vine (1966). Later, Plafker et al. (1978) estimated a rate of 58 mm/yr by measuring stream channels offset by the Fairweather fault over the past millennium. More recently, Brothers et al. (2020) mapped the fault offshore and identified a remarkable 925 m seafloor displacement of the southern margin of an ice lobe that retreated ~17,000 years ago, implying a fault slip rate of 53 ± 3 mm/yr. In contrast, the geodetic block model of Elliott and Freymueller (2020) estimates Fairweather fault slip rates that increase north to south from 35 to 46 mm/yr

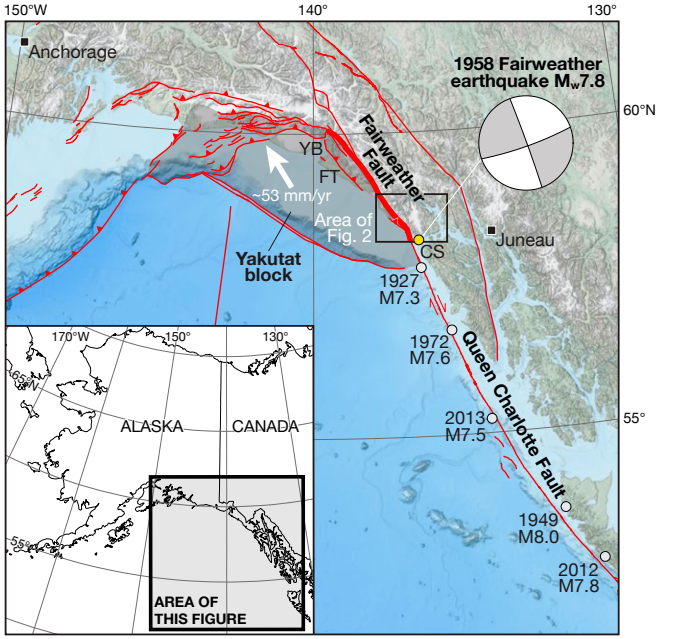

Figure 1. Tectonic setting of southeast Alaska showing the location of the Fairweather fault. Yellow circle marks the epicenter of the 1958 M_w7.8 Fairweather fault earthquake near Cross Sound, including focal mechanism (Doser and Lomas, 2000); bold red line delineates the approximate rupture length. Yakutat block moves northwest relative to North America at a rate of ~53 mm/yr (Elliott and Freymueller, 2020). YB—Yakutat Bay; FT—Foothills thrust fault; CS—Cross Sound. Earthquake ($M_w \geq 7$) epicenters along the Queen Charlotte–Fairweather fault system retrieved from https://earthquake.usgs.gov/earthquakes/search/. Source of basemap: General Topographic Chart of the Oceans (GEBCO); National Oceanic and Atmospheric Administration (NOAA) National Centers for Environmental Information (NCEI).

and require transpression along the eastern margin of the Yakutat block, as reverse faulting beneath the coastal foothills (Fig. 2).

Seismological and structural observations indicate partitioning of relative plate motions onto strike-slip and reverse faults north of Cross Sound (Fig. 1), where the southeastern edge of the Yakutat block first impinges on southeast Alaska. South of Cross Sound, the offshore Queen Charlotte–Fairweather fault strikes ~337°, and historical earthquakes near Sitka show slip aligned with the Pacific–North American plate boundary and no slip partitioning (Doser and Lomas, 2000). In contrast, north of Cross Sound, the onshore Fairweather fault strikes 10°–30° more westerly. The onshore fault bend imposes a convergent geometry oblique to Yakutat block motion (Brothers et al., 2020). This fault section ruptured in 1958, where the mainshock and aftershocks show that seismic slip occurred on steep strike-slip plate boundary faults as well as thrust faults on and offshore (Doser and Lomas, 2000; Bruhn et al., 2004).

[1]Supplemental Material 1. GIS material includes four shapefiles depicting geomorphic lines, fault lines, unit contacts, and geologic units mapped on lidar-based digital elevation models and in the field as explained in the paper. Please visit https://doi.org/10.1130/GEOS.S.13697059 to access the supplemental material, and contact editing@geosociety.org with any questions.

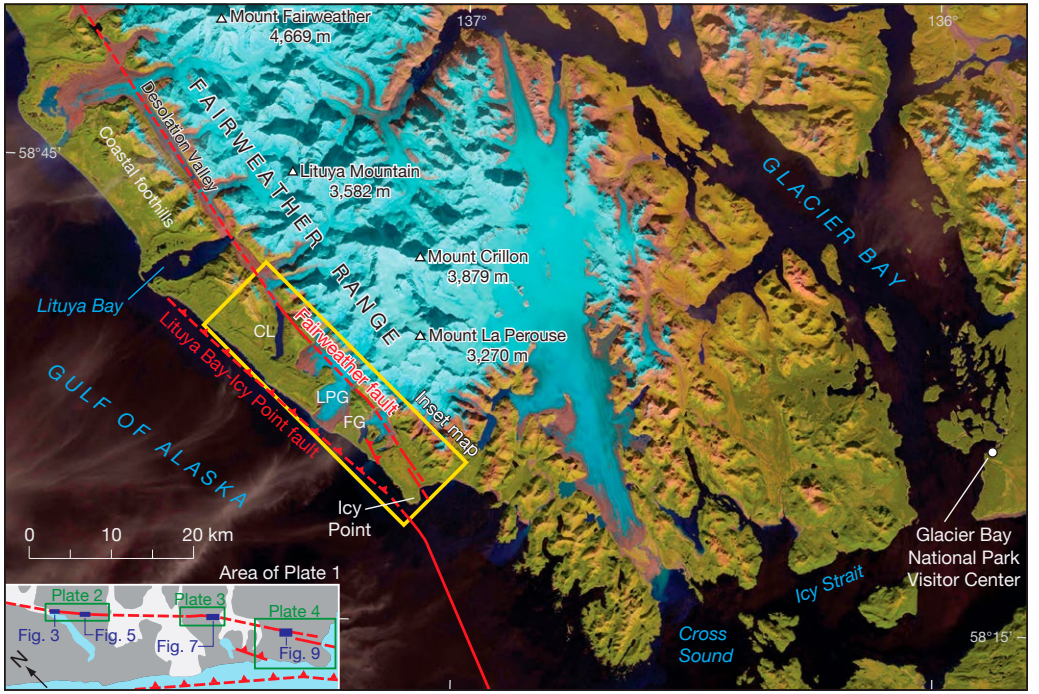

Figure 2. Landsat 8 satellite image of Glacier Bay region, acquired 22 September 2015 (U.S. Geological Survey, 2015). Solid and dashed red lines define the location of the Fairweather fault where it is well located and uncertain, respectively. Barbed red dashed lines mark the offshore Lituya Bay–Icy Point thrust fault (Plafker, 1967; Risley et al., 1992), and the Finger Glacier fault onshore. CL—Crillon Lake; LPG—La Perouse Glacier; FG—Finger Glacier. Yellow box outlines Plate 1 and the inset map in lower left. The inset map is rotated clockwise 45° and shows the locations of Plates 2, 3, and 4 and Figures 3, 5, 7, and 9.

Historical seismicity and topography along the Fairweather fault, including the prominent coastal foothills (Fig. 2), support interpretations of the eastern Yakutat block margin as a "positive flower structure" (Bruhn et al., 2004; Pavlis et al., 2004). This hypothesized structure partitions Yakutat–North America relative motion into right-lateral slip across the Fairweather fault, and northeast-directed contraction on thrust faults beneath the coastal foothills, such as the Foothills thrust fault (Fig. 1; Bruhn et al., 2004; Pavlis et al., 2004) and the Lituya Bay–Icy Point fault (Fig. 2). These observations support geodetic block models that place at least half of the convergent plate motion along a deformation zone parallel to and west of the Fairweather fault (Elliott and Freymueller, 2020). However, right-lateral-oblique slip measurements along the 1958 surface rupture and geomorphic observations described in this paper indicate that the Fairweather fault itself also accommodates rock uplift along the plate boundary.

Effects of the 1958 M7.8 Fairweather Earthquake

The 10 July 1958 Fairweather earthquake epicenter is located east of the Fairweather fault, midway between Icy Point and Cross Sound (58.31°N, 136.76°W; Doser and Lomas, 2000) (Fig. 1). The rupture propagated unilaterally toward the northwest and terminated near Yakutat Bay (Stauder, 1960; Doser and Lomas, 2000; Doser, 2010). Waveform modeling of the 1958 mainshock by Doser and Lomas (2000) determined a focal mechanism with right-lateral displacement on a fault striking 340°, dipping 88° east, at a focal depth of 16 ± 4 km. Further analysis of *P*-wave seismograms by Doser (2010) resolved four pulses of slip along a 260 km to 370 km rupture of the Fairweather fault and a magnitude of M_w 7.8. Doser (2010) estimated an average slip of 3.5 m, which compares well with horizontal fault displacements measured within a year after the 1958 earthquake (Tocher and Miller, 1959; Tocher, 1960).

Between July and September 1958 following the Fairweather earthquake, Tocher and Miller (1959) mapped surface fault displacements and earthquake-related ground failures between Crillon Lake and Icy Point. At the north end of Crillon Lake (Fig. 3), Tocher and Miller (1959) measured the greatest amount of slip: 6.5 m of right-lateral displacement and 1.1 m of west-side-up displacement across a faulted zone of shattered soil and rock ~2 m wide. Evidence for dip-slip motion was only observed along a ~250-m-long scarp near Crillon Lake (Fig. S1 in Supplemental Materal 2[2]). Elsewhere, Tocher (1960) reported predominantly right-lateral slip; any other vertical displacement, if present, was too little to detect.

Southeast of Crillon Lake, the Fairweather fault strikes through a narrow valley that separates North Dome from the higher peaks of the Fairweather Range to the east (Plate 2). Here, Tocher and Miller (1959) measured 2.7 to 3.5 m right-lateral offsets along the northeastern flank of a ~100-m-wide ridge that

Supplementary Material

Geomorphic expression and slip rate of the Fairweather fault, southeast Alaska, and evidence for predecessors of the 1958 rupture

by Rob Witter[1], Adrian Bender[2], Kate Scharer[2], Chris DuRoss[3], Peter Hacussler[1], Richard Lease[1]

[1]*U.S. Geological Survey, Alaska Science Center, 4210 University Dr., Anchorage, AK, 99508, USA*
[2]*U.S. Geological Survey, Earthquake Science Center, 525 S. Wilson St., Pasadena, CA, 91106, USA*
[3]*U.S. Geological Survey, Geological Hazards Science Center, 1711 Illinois St., Golden, CO, 80401, USA*

These supplemental files includes ten figures, five tables, and GIS map files referenced in the article. The figures include legacy photographs and a 2018 satellite image that illustrate surface deformation and geomorphic features along the Fairweather fault (Figs. S1, S2, S5, and S6). Four figures present LaDiCaoz 2.1 analyses (Zielke et al., 2015; Haddon et al., 2016) used to measure offset of stream channels and moraines that cross the Fairweather fault trace (Figs. S3, S4, S7, and S8). Fig. S9 shows a supplemental photomosaic and log of trench A after scraping ~10 cm back into the north wall. Figs. S10 and S11 present photographs and field interpretations of two test pits across the Fairweather fault adjacent to trench A at the Tocher fan site. Table S1 lists the preferred, range, and quality of horizontal offsets of landforms at the Crillon fan and Finger Glacier sites measured using LaDiCaoz. Radiocarbon analyses using OxCal Sequence models (version 4.3, Bronk Ramsey [2009]), including results and code, are shown in Tables S2–S4. Finally, GIS shapefiles that include geomorphic lineaments, surficial geologic units, unit contacts, and active faults are included with a ReadMe in a zipped compressed file.

SUPPLEMENTAL REFERENCES

Page, R., 1969, Late Cenozoic movement on the Fairweather fault in southeastern Alaska: Geological Society of America Bulletin, v. 80, p. 1873–1878.

Salisbury, J.B., Haddad, D.E., Rockwell, T., Arrowsmith, J.R., Madugo, C., Zielke, O., and Scharer, K., 2015, Validation of meter-scale surface faulting offset measurements from high-resolution topographic data: Geosphere, v. 11, p. 1884–1901, doi: 10.1130/GES01197.1.

[2]Supplemental Material 2. Ten figures and five tables that support the analyses and discussion presented in the paper. Please visit https://doi.org/10.1130/GES.S.13697290 to access the supplemental material, and contact editing@geosociety.org with any questions.

occupies the central axis of the valley. Along ridgetops adjacent to the fault valley, Tocher and Miller (1959) identified numerous parallel, uphill-facing 0.5 to 1.5-m-tall scarps and open fissures with vertical slip indicators consistent with ridgetop spreading (Plate 2).

Tocher (1960) returned in late June and July of 1959 to investigate the 1958 fault rupture at Icy Point near the mouth of Kaknau Creek (Plate 4). Several landslides along the southwest creek bank delineated a narrow zone of surface deformation that exposed unweathered bedrock, disturbed soil, and damaged trees within ~1 km of the creek mouth. Near the creek mouth, Tocher measured 3–4 m of right-lateral slip distributed over four fault strands in intensely sheared siltstone where the faults offset a tributary stream channel.

Rockfall, loosened by fault rupture or earthquake shaking in 1958, generated a mega-tsunami in Lituya Bay (Miller, 1960); this mega-tsunami remains infamous for achieving the highest wave runup in recorded history (Fritz et al., 2009). Within minutes of the 1958 earthquake, ~30.6 million m^3 of rock avalanched off the northeast wall of the bay, impacted the water at high speed (estimated at 110 m/s), drove a wall of water over the opposite ridge, and stripped the forest, exposing bedrock up to a maximum elevation of 524 m (Miller, 1960).

The following section presents summaries of the geomorphic expression of the Fairweather fault, which we mapped on three lidar DEMs (Plate 1). We describe tectonic landforms mapped in the context of surficial geology, published observations gathered immediately after the 1958 earthquake, and verification of the mapping during our fieldwork in 2016 and 2017. We also identify potential sites for paleoseismic investigation and reassess slip rates based on fault displacement of stream channels and moraines.

After summarizing our mapping, a subsequent section describes the stratigraphic and structural relations observed in hand-dug excavations that cross active fault traces at the Tocher fan site. We also present geochronological data used to reconstruct a partial history of surface-fault ruptures over the past 5600 years.

GEOMORPHIC EXPRESSION OF THE SOUTHERN FAIRWEATHER FAULT

Approach and Methods

We use new airborne-lidar–based, digital elevation models (DEMs) to map tectonic landforms and surficial geology along the southern 30 km of the Fairweather fault in unprecedented detail (Plate 1). With the support of

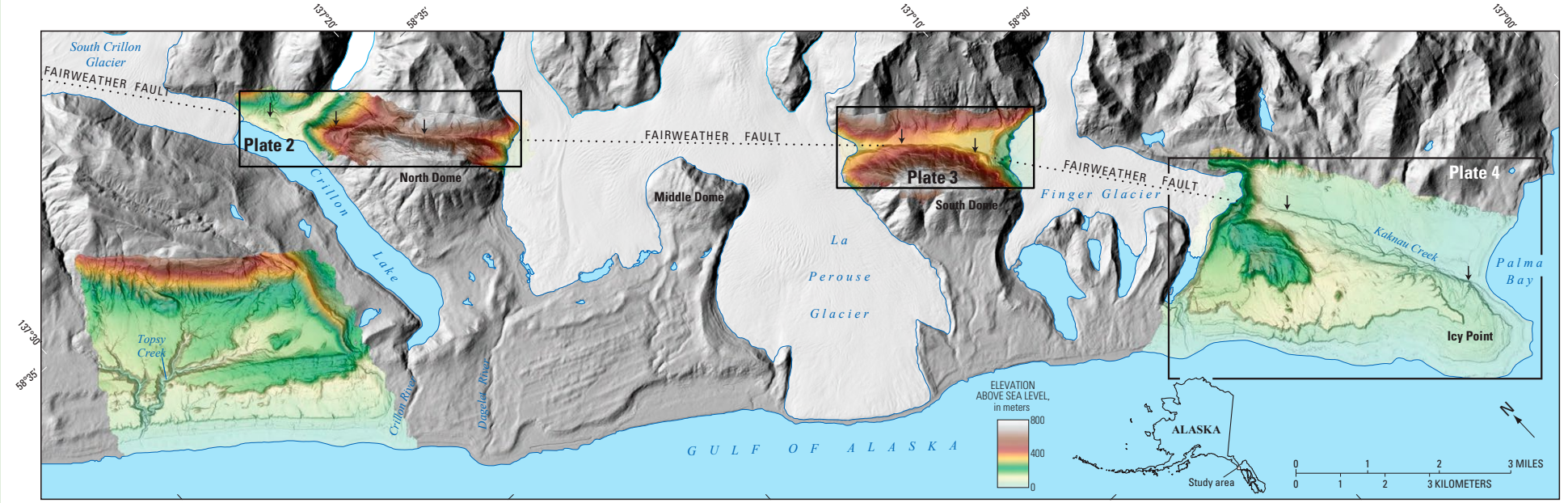

Plate 1. Map of Fairweather fault study area. Active fault scarps identified by black arrows and dotted beneath ice. Gray base map is a regional Alaska digital terrain model (DTM) with 5 m per pixel resolution (m/pixel). Four digital terrain models are shown in color as shaded-relief maps (1 m/pixel resolution) derived from light detection and ranging (lidar) data acquired in September 2015 (Witter et al., 2017a).

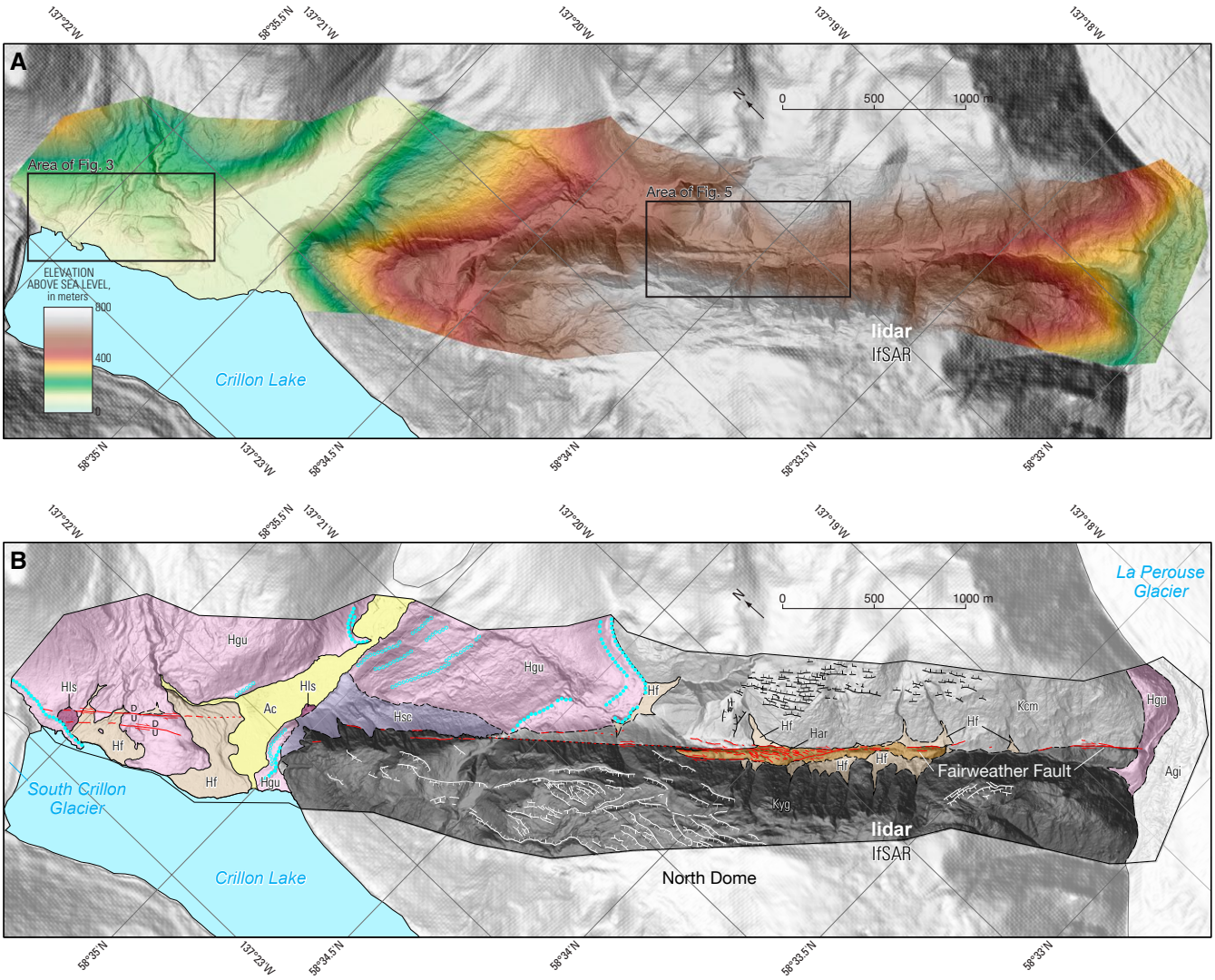

EXPLANATION

Lines

Solid - certain
Dashed - approximate
Dotted - uncertain/inferred

- Contact
- Shoreline feature
- Right-lateral strike-slip fault
- Fault showing vertical offset; U, upthrown block, D, downthrown block
- Fault showing right-lateral oblique slip; U, upthrown block, D, downthrown block
- Suspicious lineament
- Sackung; hachures point uphill
- Moraine crest; hollow where poorly expressed

Map units

Ab	Active beach	Hsc	Slope colluvium
Ac	Active channel	Hsr	Shutter ridge
Agi	Glacier ice	Har	Axial ridge
Hf	Alluvial/colluvial fan	Hmt-A	Marine terrace A
Hbr	Beach ridge	Hmt-B	Marine terrace B
Hds	Dune	Pmt-C	Marine terrace C
Hdt	Death River terraces	Pmt-D	Marine terrace D
Hgu	Glacial landform, undivided	Pfe	Alluvial/colluvial fan, east of fault
Hkt	Kaknau Creek terraces	Pfw	Alluvial/colluvial fan, west of fault
Hls	Landslide deposit	Tty	Topsy/Yakataga Formation rocks, undivided
Hpa	Ponded alluvial sediment	Kcm	Chugach metamorphic rocks, undivided
		Kyg	Yakutat Group rocks, undivided

A - active; H - Holocene; P - Pleistocene; T - Tertiary; K - Cretaceous

Plate 2. (A) Shaded relief map derived from light detection and ranging (lidar) topography acquired between Crillon Lake and La Perouse Glacier. (B) Map of surficial geology and active traces of the Fairweather fault between Crillon Lake and La Perouse Glacier. North orientation rotated 48°. IFSAR—interferometric synthetic aperture radar.

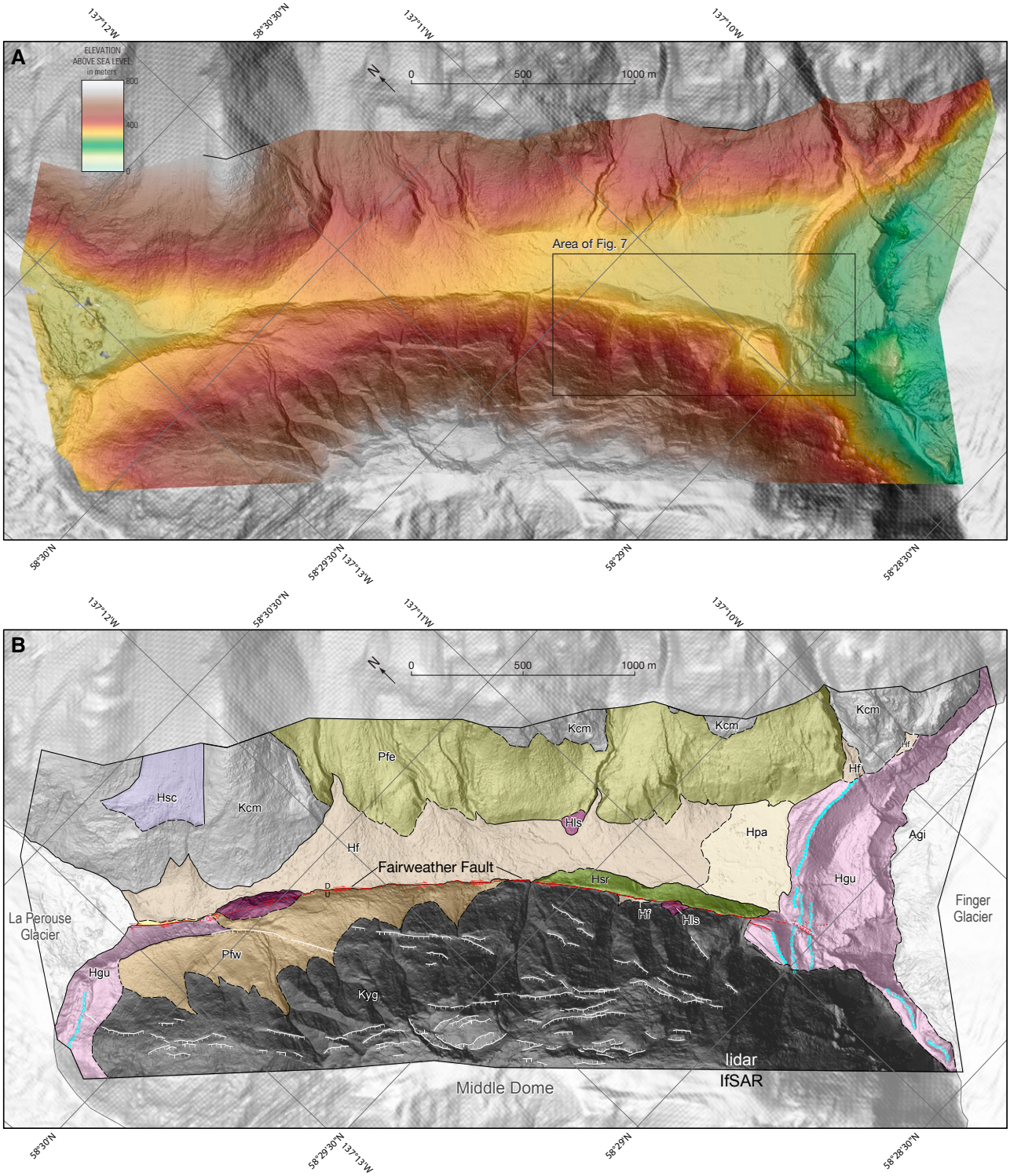

Plate 3. (A) Shaded relief map derived from light detection and ranging (lidar) topography acquired between La Perouse Glacier and Finger Glacier. (B) Map of surficial geology and active traces of the Fairweather fault between La Perouse Glacier and Finger Glacier. See Plate 2 for explanation of surficial geologic units and fault symbology. North orientation rotated 48°.

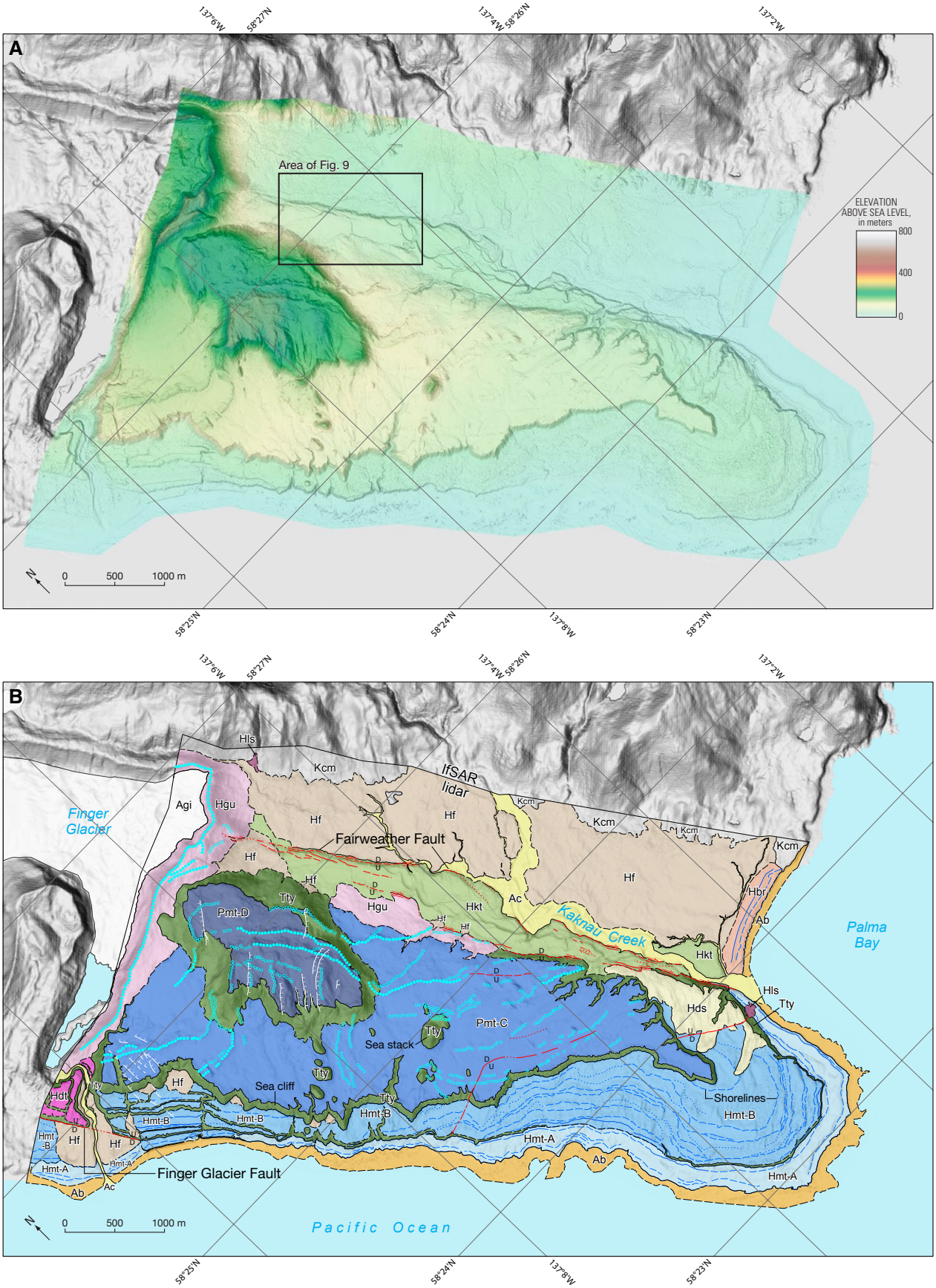

Plate 4. (A) Shaded relief map derived from light detection and ranging (lidar) topography acquired between Finger Glacier and Icy Point. (B) Map of surficial geology and active traces of the Fairweather fault between Finger Glacier and Icy Point. See Plate 2 for explanation of surficial geologic units and fault symbology. North orientation rotated 48°.

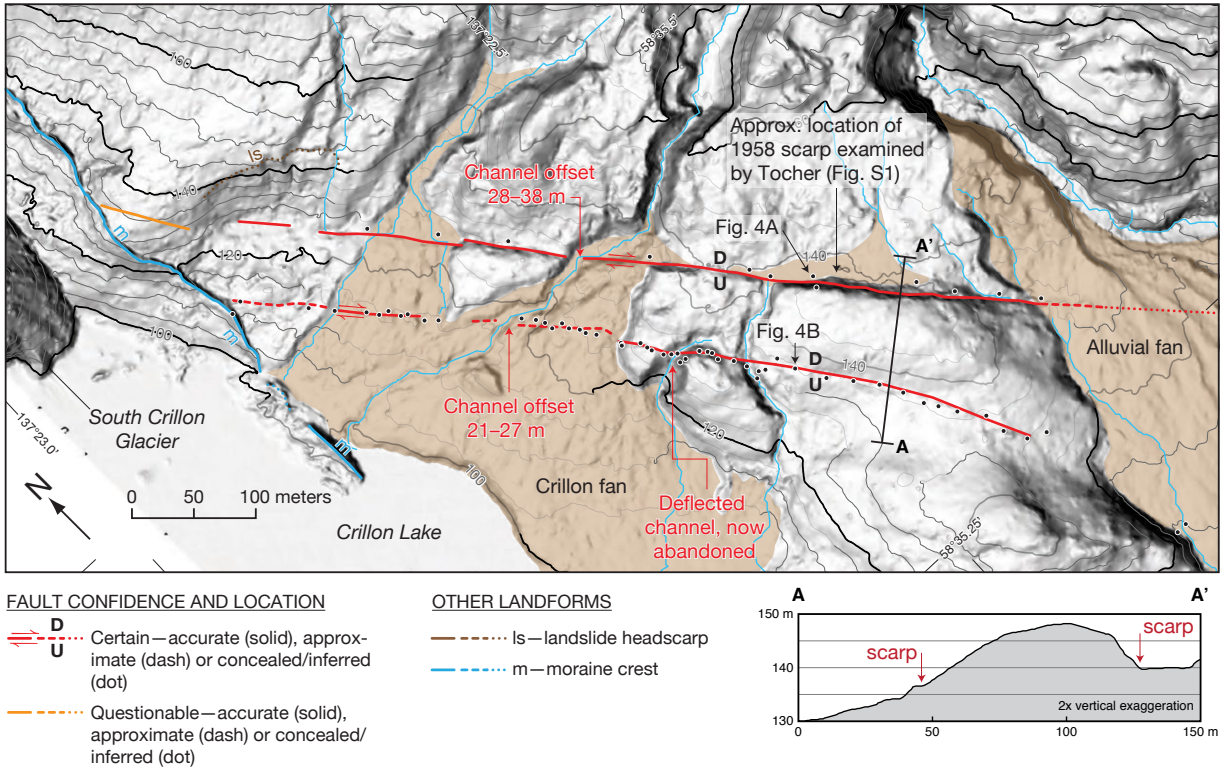

Figure 3. Map of active fault traces and other landforms revealed by light detection and ranging (lidar) at the Crillon fan site. Contour interval is 5 m. Location of map shown on Plate 2. Two uphill-facing scarps offset stream channels and glacial deposits along the northeastern shore of Crillon Lake. The most prominent (eastern) fault trace forms an 8-m-high scarp (field checked at black dots) and slipped 6.6 m horizontally and 1.1 m vertically in the 1958 earthquake. A more subtle (western) fault trace produced 1–1.5 m of horizontal and ~0.5 m of vertical displacement that we verified in the field (black dots). Alluvial fans colored tan. Other lines delineate landslides and moraines by color and also denote prominent (solid), clear (dash), and subtle (dot) geomorphic expression. Recent advances of the South Crillon Glacier are presented in Figure S2 [footnote 2]. Channel offset measurements shown on Figures S3 and S4.

the National Park Service, and in collaboration with the Army Corps of Engineers, Cold Regions Research and Engineering Laboratory (CRREL), and the National Center for Airborne Lidar Mapping (NCALM), we acquired >166 km^2 of high-resolution airborne lidar data. CRREL developed and deployed the Helipod lidar system, designed for use on a Robinson R44 Raven II helicopter, to acquire more than 34.4 million laser measurements. The measurements have vertical and horizontal accuracies of ±0.10 m. We used the "bare-Earth" point cloud with 1.4–2.3 returns per square meter, provided by NCALM, to produce 1-m-per-pixel DEMs for three sections of the fault between Crillon Lake and Palma Bay (Witter et al., 2017a, 2017b).

We followed the approach of Wallace (1990) to map and characterize the geomorphic expression of active fault-related landforms evident on three lidar DEMs (Plates 2–4) using standard geographic information system tools. The locations of the three lidar DEMs are shown on Plate 1, including the northern (Plate 2), middle (Plate 3), and southern (Plate 4) lidar DEMs. To enhance our interpretation of lidar DEMs, we also consulted aerial photography, ~1-m-resolution DigitalGlobe satellite imagery, and 5-m-resolution digital topography derived from interferometric synthetic aperture radar (U.S. Geological Survey, 2016). We use the MATLAB-based displacement calculator LaDiCaoz 2.1 (Zielke and Arrowsmith, 2012; Zielke et al., 2015; Haddon et al., 2016) to measure

lateral displacement of landforms (e.g., stream channels and moraines) across mapped fault traces.

We field-checked the lidar maps during aerial reconnaissance and at field sites near Crillon Lake and at Icy Point. We surveyed landforms using a TRIMBLE Geo7x mapping-grade Global Navigation Satellite Systems (GNSS) instrument to provide sub-meter accuracy. GNSS data were post-processed using TRIMBLE software and the nearest National Geodetic Survey Continuously Operating Reference Station (CORS), AB43, at Cape Spencer, Alaska. In June 2016, we verified the location of the uphill-facing primary fault scarp first identified by Tocher and Miller (1959) and measured displacement along a previously unrecognized secondary fault in the same area that we discovered in lidar maps (Fig. 3 and Plate 2). We also field-checked lineaments and landforms mapped on lidar at the pervasively fractured axial ridge described by Tocher (1960) east of North Dome. Fieldwork in May 2017 included surveys to verify the elevations of marine terrace shorelines mapped on lidar at Icy Point and fault-related landforms in the heavily vegetated Kaknau Creek valley.

We use OxCal (version 4.3.2, Bronk Ramsey, 2009) and the IntCal13 atmospheric ^{14}C curve (Reimer et al., 2013) to calibrate ^{14}C ages reported in this study and ages published by Plafker et al. (1978), which constrain ages of stream channels and moraines offset by the Fairweather fault. We report calibrated ^{14}C ages in years before 1950 Common Era (CE) (Table 1); these ages result from correcting lab-reported ^{14}C ages to account for variations in atmospheric ^{14}C concentrations over time. The full radiocarbon data release is available in Witter and Bender (2020).

Crillon Lake to La Perouse Glacier

The northern lidar DEM covers an ~1.5-km-wide swath that extends ~6.5 km along the Fairweather fault from the northeast shore of Crillon Lake to the southeast where it intersects La Perouse Glacier (Plate 2). Using detailed lidar topography, we reexamined the geomorphic expression of active fault traces, compared our map to post-1958 investigations (Tocher and Miller, 1959; Tocher, 1960; Plafker et al., 1978), and identified potential sites for paleoseismic analyses. We identified two sites for detailed field investigations: the Crillon fan site and the Tocher fan site. Field investigations checked the location, length, and vertical separation of fault scarps that ruptured in 1958, verified a previously unidentified secondary scarp, and reassessed stream channel offsets first measured by Plafker et al. (1978) to estimate the late Holocene lateral slip rate.

Crillon Fan Site

Along the northeastern shore of Crillon Lake (Fig. 3 and Plate 2), a conspicuous cleft in the forest (Fig. S2 [footnote 2]) defines where the active trace of the Fairweather fault cuts across a late Holocene alluvial fan (Hf, see explanation in Plate 2), here informally named Crillon fan. Tocher and Miller (1959) discovered an 8-m-high, uphill- (northeast-) facing fault scarp that reactivated during the 1958 earthquake, producing 6.5 m right-lateral and 1.1 m vertical offsets. This prominent scarp trends northwest (321°) and continuously disrupts the fan surface over a distance of 830 m with vertical separation of 1–8 m (Fig. 4A). We observed tilted, toppled, and drowned trees, as described by Page (1969), along the entire length of this fault strand. The fault right-laterally offsets three stream channels and forms barriers that pond alluvial gravel uphill of the scarp. Coarse, unconsolidated alluvium and a shallow water table made this site unsuitable for paleoseismic excavation. To the northwest, the scarp ends at a moraine of the South Crillon Glacier (Fig. 3); this moraine advanced between 1959 and 1975, erasing evidence for surface fault rupture north of the moraine (Fig. S2 [footnote 2]). Densely vegetated alluvial fan deposits conceal the fault trace to the southeast.

About 50 m southwest of the 8-m-high scarp measured by Tocher (1960), lidar revealed a previously unmapped secondary scarp (Fig. 3). The secondary scarp parallels the larger scarp, faces uphill to the northeast, and displaces the fan surface over a distance of 660 m with a vertical separation of ~0.5 m. Tilted and fallen trees across the secondary scarp (Fig. 4B) suggest recent surface-fault rupture consistent with slip during the 1958 earthquake. If the secondary scarp also ruptured in 1958, then the total vertical displacement on the two fault strands taken together exceeded 1.5 m. Lateral displacement in 1958 also may have been greater than reported: our field measurements identified ~1 m offsets of recent stream channel margins along the secondary scarp. Additional stream channels deflected by the secondary scarp (Fig. 3) imply a history of fault displacement prior to 1958.

Right-lateral displacements on two strands of the Fairweather fault have offset the central stream channel on Crillon fan. We use LaDiCaoz to correlate cross sections of channels offset along the primary and secondary Crillon fan fault scarps. Reconstructions indicate 28–38 m offset of the central channel across the primary fault scarp and 21–27 m offset across the secondary fault scarp (Fig. 3; Figs. S3, S4, and Table S1 [footnote 2]). Total offset across both fault traces ranges from 49 to 65 m (Table 2).

To derive a slip rate from observations at the Crillon fan site, we use ages published by Plafker et al. (1978) from the lateral moraine of the South Crillon Glacier. The moraine provides a maximum constraint on the age of the fan because it defines the most recent ice advance into the Crillon Lake basin and predates the subsequent development of stream channels after ice retreat (Plafker et al., 1978) (Fig. 3 and Table 1). An OxCal Sequence model (OxCal version 4.3, Bronk Ramsey, 2009) for soils buried by the lateral moraine constrains the age of the fan formation to no earlier than 1000 cal. yr B.P. (Fig. S3 and Table S2). This maximum age constraint, divided into the full range of measured channel offsets (49–65 m), indicates a minimum slip rate ≥49 mm/yr (Table 2). We compare this revised slip rate (≥49 mm/yr) to published estimates in the Discussion section.

TABLE 1. RADIOCARBON DATES AND CALIBRATED AGE RANGES FOR SAMPLES FROM TOCHER FAN SITE ON THE FAIRWEATHER FAULT, GLACIER BAY NATIONAL PARK, ALASKA

Calibrated age (2σ cal. yr B.P.)*	Analytical age (1σ ^{14}C yr B.P.)†	Accession number	Sample name	Stratigraphic context	Material dated§
Plafker et al. (1978)#					
1270–560	940 ± 200	—	W-3313	Soil horizon SC2	Wood
4800–3340	3600 ± 250	—	W-3305	Soil horizon SC1	Wood
6180–5050	4880 ± 200	—	W-3311	Soil horizon SC1	Peat
1690–800	1320 ± 200	—	W-3307	Soil horizon F3	Wood
4780–3260	3580 ± 250	—	W-3303	Soil horizon F2	Wood
4570–3480	3670 ± 200	—	W-3310	Soil horizon F2	Peat
7160–5930	5670 ± 250	—	W-3312	Soil horizon F1	Wood
8380–7490	7060 ± 250	—	W-3322	Soil horizon F1	Wood
8510–7570	7170 ± 250	—	W-3323	Soil horizon F1	Wood
9890–8380	8160 ± 300	—	W-3306	Soil horizon F1	Peat
Tocher Fan gouge core TP-4					
260–20	105 ± 20	OS-130999	TP-4 moss	Buried peat at 1.07 m	Peat moss
290–0	175 ± 20	OS-130998	TP-4 seeds	Buried peat at 1.07 m	Herbaceous seeds
Trench A					
510–460	410 ± 15	OS-130796	TPAS-3	South wall, unit 4	Two conifer twigs
900–740	880 ± 15	OS-139775	TPAS-6	South wall, unit 6	Conifer needles
4520–4420	3990 ± 25	OS-139774	TPAS-2	South wall, unit 6	Conifer needles
4830–4620	4170 ± 20	OS-130208	TPAS-1	South wall, unit 8	Detrital wood
4860–4730	4240 ± 20	OS-130209	TPAS-5	South wall, unit 8	Detrital wood
5640–5580	4860 ± 20	OS-130430	TPAN-7	North wall, unit 9	Detrital wood
Test pit B					
1040–930	1060 ± 15	OS-139776	TPBS-4	South wall, unit 2	Twig with bark
Trench D					
540–510	505 ± 15	OS-130432	TPDS-10	South wall, unit E	Conifer needles
890–730	875 ± 15	OS-130797	TPDS-3	South wall, unit B soil	Conifer twigs
900–740	880 ± 15	OS-130433	TPDS-4	South wall, unit Da	Conifer needles
1280–1180	1270 ± 25	OS-130481	TPDS-5	South wall, unit C	Detrital wood
1700–1560	1710 ± 20	OS-130482	TPDS-2	South wall, unit A	Detrital wood
1780–1620	1780 ± 15	OS-139777	TPDS-8	South wall, unit A	Detrital wood
3170–3060	2950 ± 15	OS-130939	TPDS-1	South wall, unit A	Detrital wood

Note: Dashes indicate "not available" or "not recorded."

*Calibrated ages in years before 1950 CE rounded to nearest decade were calculated using OxCal (version 4.3.2, Bronk Ramsey [2009]; 95% probability distribution at 2σ) with the IntCal13 dataset of Reimer et al. (2013).

†Age calculated using a radiocarbon half-life of 5568 years and reported at one standard deviation in radiocarbon years before 1950 CE by the National Ocean Sciences Accelerator Mass Spectrometry Facility, Woods Hole, Massachusetts, USA.

§Samples, except peat moss, are detrital, so the accelerator mass spectrometer ages are maximum ages for sediment at the depth of the sample.

#See table 1 in Plafker et al. (1978) for detailed description of sample provenance and interpretations.

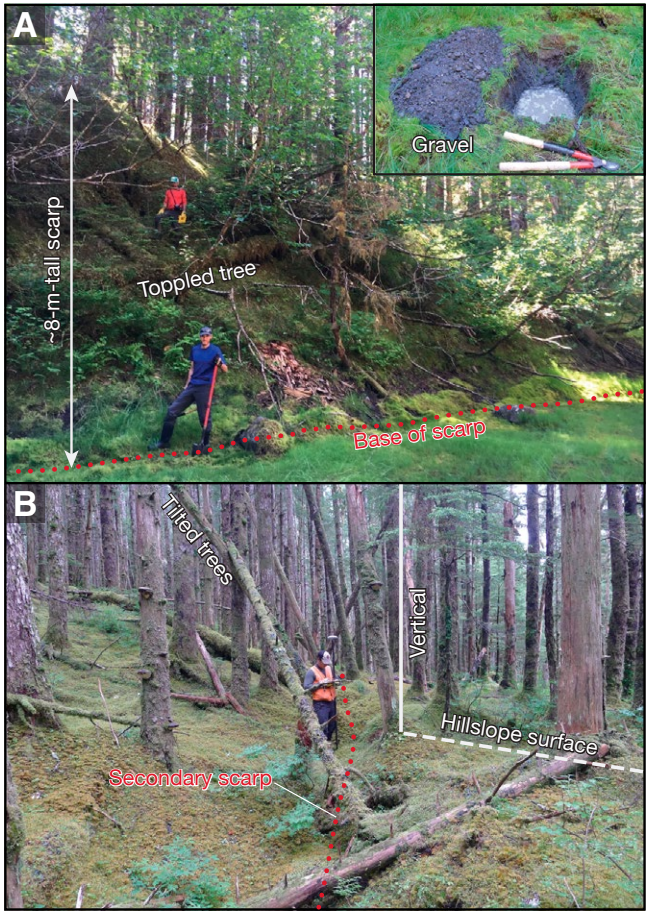

Figure 4. (A) Coarse sediment and shallow groundwater (inset photo) prevented trenching across uphill-facing scarps (up to 8 m tall) on the eastern fault trace at the Crillon Lake site. (B) West of the primary fault scarp, we mapped a secondary fault scarp (red dotted line) with ~1 m dextral and ~0.5 m vertical offsets; tilted and fallen trees along the scarp imply slip in 1958.

Tocher Fan Site

The Tocher fan site, ~500 m above Crillon Lake and ~3 km southeast of the Crillon fan site, occupies a narrow fault-strike–parallel valley between North Dome and the higher mountains of the Fairweather Range (Plate 2). The site is named for an alluvial fan (Hf) flanking the eastern margin of an axial ridge (Har; Fig. 5 and Plate 2) that was disrupted by numerous fractures during the 1958 earthquake (Tocher and Miller, 1959; Tocher, 1960). Tocher (1960) also identified a small pond impounded by the 1958 scarp; the pond drained before our overflight in 2015, revealing alluvial fan deposits (Fig. 6). We selected this site for paleoseismic trenching (described in a subsequent section) to more closely examine a 1958 primary surface fault rupture along the northeastern bounding "fracture" (Fig. S5), which right-laterally displaced fallen logs and tree stumps by 2.7–3.5 m as described by Tocher (1960, p. 282):

> "This nearly continuous fracture lay on but near the base of the northeast slope of the low axial ridge. Many other fractures were formed higher on the northeast slope, near the crest, and part way down the southwest slope of the ridge. The measured offsets of these logs therefore represent only an indeterminate fraction of the total fault movement east of North Dome. Many of the other fractures on the ridge were open, and the lengths of many could be measured in hundreds of feet."

We used GNSS surveys at the Tocher fan site to field-check tectonic geomorphic features interpreted on lidar maps, measure topographic profiles across the axial ridge, and define fault scarps and fractures that shatter the ridge crest. The axial ridge rises 10–15 m above prominent geomorphic lineaments (e.g., linear swales, scarps, and slope breaks) that define its eastern and western margins, based on lidar and GNSS-surveyed profiles (Fig. 6). Survey observations replicated the lidar profiles of the axial ridge, except where dense vegetation decreased GNSS survey accuracy of field measurements. The ~1100-m-long axial ridge is 45–90 m wide near its middle and tapers toward both ends (Figs. 5 and 6).

We infer that the positive topography of the axial ridge results from contraction between two or more fault strands with oblique, transpressional geometries. Scarps that bracket the axial ridge are oriented 22°–32° more westerly than the direction of relative motion between the Yakutat block and North America. One or more northeast-facing fault scarps, 4–12 m high and trending 315°, define the eastern margin of the ridge, which coincides with the 1958 "continuous fracture" observed by Tocher (1960) (Fig. S5 [footnote 2]). A linear, 5–15-m-tall scarp that trends 305° defines the southwest-facing southern flank of the axial ridge. We propose that the contractional geometry, vertical separation, and positive topography expressed by this set of scarps reflect right-lateral, oblique-reverse faulting that has pushed up a local transpressional ridge. The north-northwest–oriented open fractures that shattered the axial ridge in 1958 (e.g., orange lines in Fig. 5; Tocher, 1960) may reflect coseismic extensional fractures oriented subparallel to the principal horizontal stress axis.

Northwest of the Tocher fan site, fault-related geomorphic features consist of sparse, discontinuous linear benches etched into steep, northeast-facing bedrock cliffs at the north end of North Dome (Plate 1). Landslides along these cliffs obscured the surface trace of the 1958 rupture according to Tocher (1960). South of the site, discontinuous linear valleys and slope breaks define active strands of the Fairweather fault until it disappears under the La Perouse Glacier. Ridge-parallel, uphill-facing scarps and troughs in bedrock above the Tocher fan site (Fig. S6), recognized in 1958 by Tocher (1960), are also evident in lidar

TABLE 2. FAIRWEATHER FAULT SLIP RATES ESTIMATED FROM OFFSET GEOMORPHIC FEATURES

Landform	Estimated age of landform (cal. yr B.P.)	Lateral offset (m)		Slip-rate using offset range (mm/yr)
		Preferred	Range	
Crillon fan middle channel	≤1000*	57†	49–65†	≥49§
Finger Glacier high moraine	1610–4080#	112	105–116	26–72
Finger Glacier recessional moraine	≤1400#	43	38–47	≥27§

*Maximum age constraint using OxCal sequence model (Table S2 [text footnote 2]).
†Lateral displacement estimated across primary and secondary fault strand at Crillon fan site (Figs. S3 and S4 and Table S1).
§Minimum slip-rate estimate based on maximum age constraint.
#Age constrained by maximum- and minimum-limiting radiocarbon dates using OxCal sequence model (Table S3).

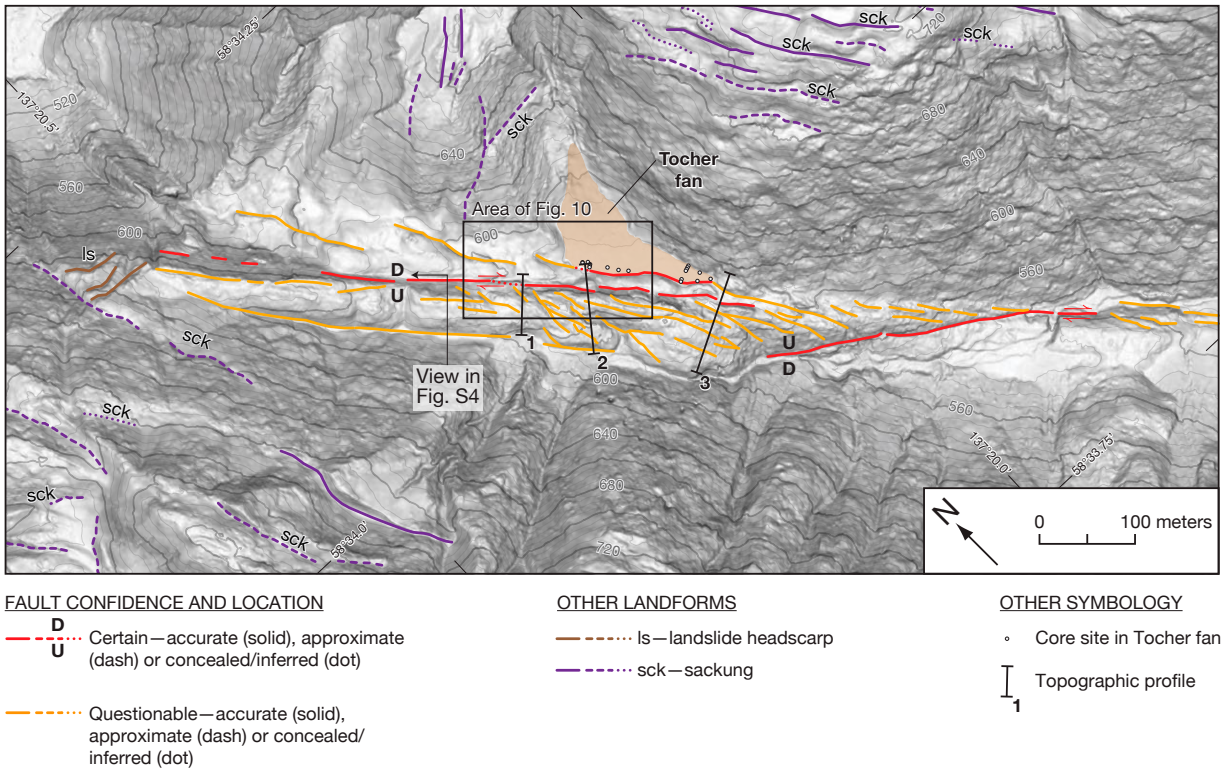

Figure 5. Map of active fault traces and other landforms revealed by light detection and ranging (lidar) at the Tocher fan site. Location of map shown on Plate 2. Our trenching site (Fig. 10) focused on evidence for active faulting along an axial ridge in a fault-parallel valley located ~3 km southeast of the Crillon Lake site. Lidar topography and field observations indicate that the Tocher fan is bounded by northeast-facing fault scarps along the base of the axial ridge. A narrow linear trough bounds the ridge to the west, and numerous NNW-trending lineaments cut the ridge between the most prominent scarps that delineate the east and west margins of the ridge. Other landforms indicated by colored lines denote prominent (solid), clear (dash), and subtle (dot) geomorphic expression. Profile locations 1, 2, and 3 correspond with topographic profiles provided in Figure 6. Contour interval is 5 m.

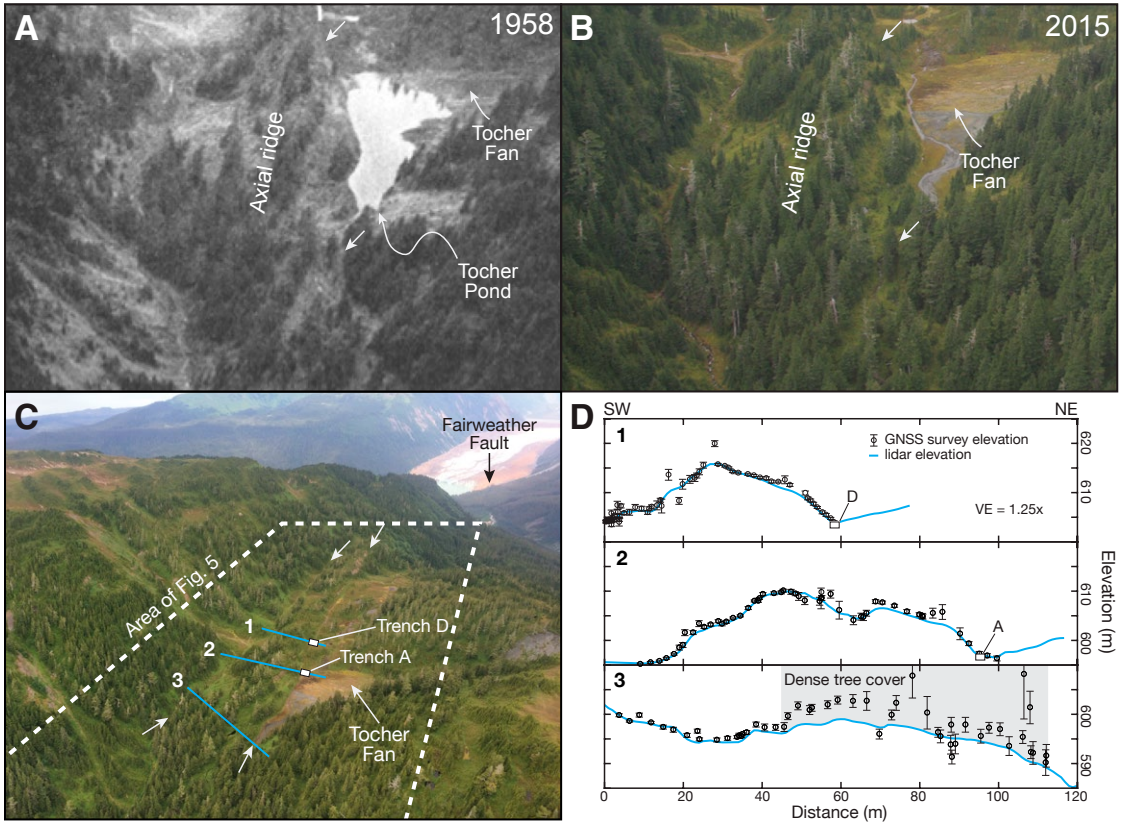

Figure 6. Oblique aerial images of the Tocher fan site looking to the northwest. (A) An oblique air photo from 1958 by Tocher (1960) shows a pond impounded by the east-facing scarp that borders the eastern margin of the axial ridge. Arrows indicate base of the east-facing scarp. (B) No pond was present in 2015 when we visited the site. An alluvial fan filled the pond sometime after 1958. The fan abuts the east side of the axial ridge, and a small creek drains the basin through a low gap in the scarp to the south. Arrows indicate location of east-facing scarp. (C) Oblique air photo of the Tocher fan site taken in 2016. White arrows indicate the western west-facing scarp and eastern narrow linear trough that bound the axial ridge. Numbers 1, 2, and 3 indicate elevation profiles across the axial ridge and bounding scarps. (D) Southwest to northeast elevation profiles across the axial ridge and bounding scarps, with numbers referencing profile lines on Figures 5 and 6C. Dense tree cover along profile 3 increased errors in Global Navigation Satellite Systems (GNSS) survey points collected to field check light detection and ranging (lidar).

on both sides of the fault (Fig. 5 and Plate 2) and probably represent sackungen (sck)—ridgetop scarps activated by seismic shaking and gravitational spreading (e.g., Radbruch-Hall et al., 1976).

La Perouse Glacier to Finger Glacier

The middle lidar DEM covers a 1.5-km-wide, 4.5-km-long swath that resolves a narrow Fairweather fault trace between the La Perouse Glacier and Finger Glacier (Plate 3). In the northern part of the lidar map, ice, alluvial, and landslide deposits cover or obscure the Fairweather fault trace for more than 1200 m. In the central part of the valley, we map the active fault trace along an east-facing, 4–5-m-high, curvilinear scarp that juxtaposes steep older fan surfaces (Pfw) on the west against younger Holocene fans (Hf) on the east. In the southern part of the map, a single, nearly continuous lineament follows a narrow trough between a shutter ridge (Hsr) on the east and the lower flank of South Dome to the west (Fig. 7 and Plate 3). The well-defined fault trace along the shutter ridge splays into three lineaments that cut across and appear to right-laterally displace moraines of Finger Glacier. Abundant sackungen occur above the fault and form uphill-facing scarps and linear troughs on the eastern side of South Dome (Plate 3).

We combine right-lateral offsets of Finger Glacier moraines evident in lidar with age data published by Plafker et al. (1978) to provide additional constraints on Fairweather fault-slip rates. Exposed lateral moraine sections described by Plafker et al. (1978) include boulder till separated by buried soils that contain wood and peat. The stratigraphy described implies successive, spatially coincident moraines that record three Holocene advances of Finger Glacier. Radiocarbon ages published by Plafker et al. (1978), listed in Table 1, serve as limiting constraints on ages of the moraines. We use an OxCal Sequence model (Table S3; OxCal version 4.3, Bronk Ramsey, 2009) of ^{14}C ages on wood

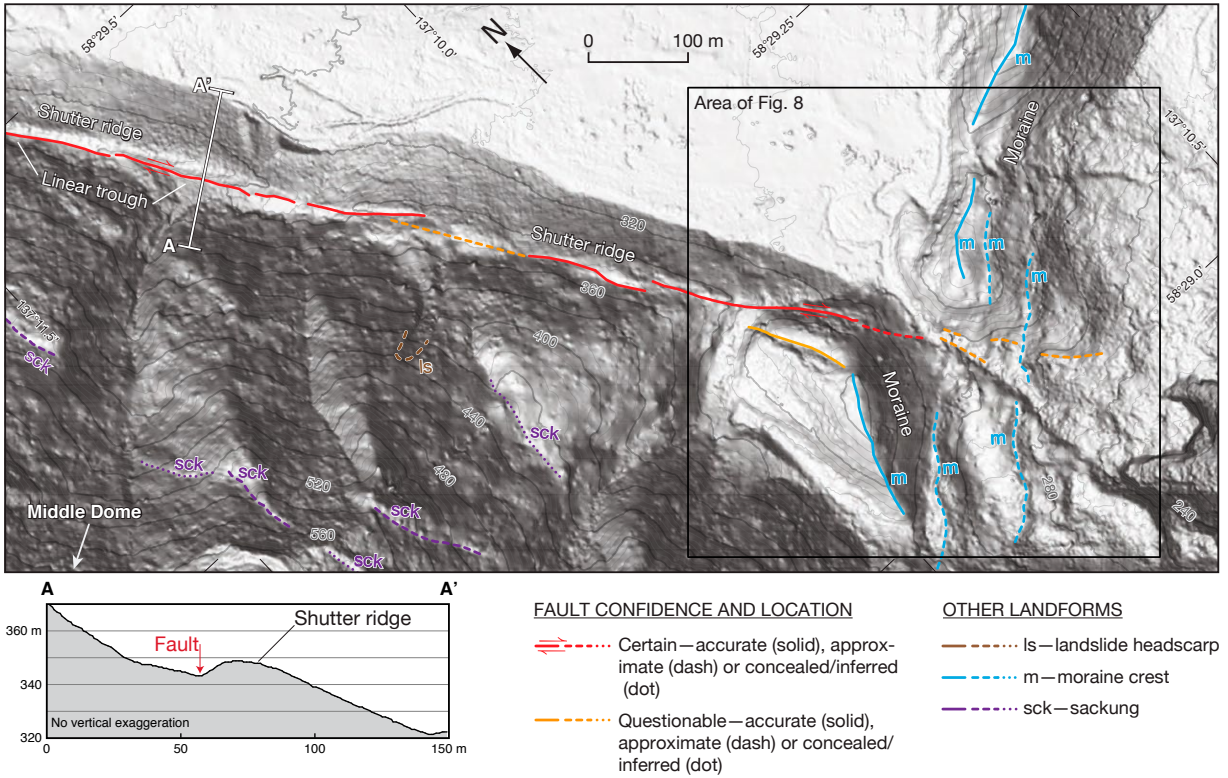

Figure 7. Map of active fault traces and other landforms revealed by light detection and ranging (lidar) near the northern Finger Glacier lateral moraine. Location of map shown on Plate 3. Northwest of Finger Glacier, tectonic lineaments resolve active traces of the Fairweather fault within a narrow zone. Linear valleys, side-hill benches, and southwest-facing scarps separate a shutter ridge from the eastern flank of Middle Dome. Other landforms indicated by colored lines denote prominent (solid), clear (dash), and subtle (dot) geomorphic expression. For example, lidar reveals uphill-facing scarps and troughs caused by ridgetop spreading (sck). Lateral moraines of Finger Glacier are right-laterally offset on the southeast side of the map. Profile A–A′ shows an uphill-facing fault scarp that traps alluvial fan sediment behind a prominent shutter ridge. Contour interval is 5 m.

and peat collected from buried soils to estimate a 1620–4080 cal. yr B.P. age for the high moraine and a maximum age of 1400 cal. yr B.P. for a younger recessional moraine (Table 2). We use LaDiCaoz to measure a 112 m offset of the Finger Glacier high moraine (preferred estimate in Table 2) with a range of 105–116 m (Figs. 8 and S7 [footnote 2]). Measured offset of a younger recessional moraine ranges from 38 to 47 m with a preferred offset of 43 m (Fig. S8 and Table 2). The age of the high moraine divided into the full range of possible offset measurements results in a slip rate of 26–72 mm/yr (Table 2). Because ^{14}C data provide only maximum constraints on the age of a younger recessional moraine, the minimum slip rate estimated with the full range of offset measurements is ≥27 mm/yr (Table 2). Slip rates estimated from offset Finger Glacier moraines, although imprecise, encompass estimates from offset channels on Crillon fan. A comparison of these rates with published slip-rate estimates will be presented in the Discussion section.

Kaknau Creek Section and Terraces at Icy Point

The southern lidar DEM extends 4 km inland from the coast, across a flight of late Quaternary marine terraces and covers 8 km of the Fairweather fault from the southern moraine of Finger Glacier to where the fault extends offshore at Icy Point (Plate 4). Unlike the northeastern lateral moraine of Finger

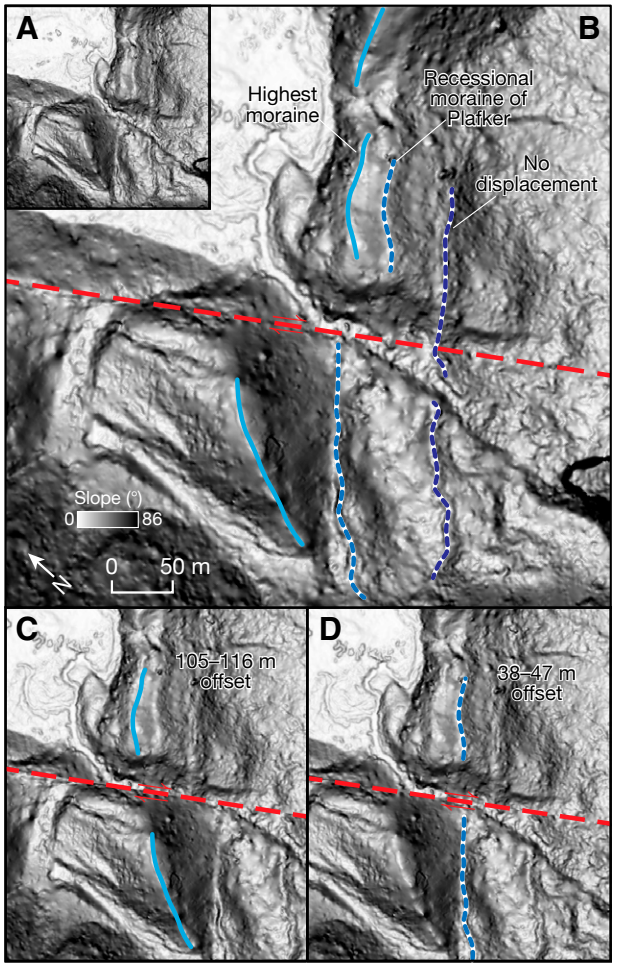

Figure 8. (A) Lateral moraines of Finger Glacier offset by the Fairweather fault provide broad constraints on slip rate. Lidar topography of the Fairweather fault near the Finger Glacier moraine shows a distinct uphill-facing scarp and shutter ridge along the western valley margin. (B) The fault offsets multiple moraine ridge crests. (C and D) Reconstructions of the Finger Glacier lateral moraines. We used LaDiCaoz software (Figs. S7 and S8 [see text footnote 2]; Zielke and Arrowsmith, 2012; Zielke et al., 2015) to estimate a 105–116 m offset of the oldest moraine along the projected fault trace (in C), and a 38–47 m offset of a younger moraine, which is slightly less than the 50 m minimum offset reported by Plafker et al. (1978) (in D).

Glacier, we observe no fault displacement of its southern moraine, which suggests recent modification by ice may have obscured faulting. Linear scarps, slope breaks, and landslides reflect active faulting along the west bank of Kaknau Creek where a flight of stream terraces (Hkt) flank the western valley margin, but stream terraces are conspicuously absent on the east side of the valley (Figure 9 and Plate 4). Near the creek mouth, dune sand (Hds) mantles the stream terraces where they adjoin shorelines that evidence the episodic emergence of marine terraces (Hmt) beveled into Icy Point (Plate 4). East-facing scarps along the west side of the valley measure as tall as 25 m (Fig. 9) and step right across inset stream terraces to a scarp near the mouth of Kaknau Creek, where Tocher (1960) measured 2.5–4 m of right-lateral slip in the 1958 earthquake (Plate 4). Tocher did not observe vertical separation on scarps bordering Kaknau Creek and recorded no uplifted stream or marine terraces formed during the earthquake, indicating the 1958 rupture produced little, if any, vertical displacement of Icy Point. During field investigations in 2017, we revisited the stream channel where Tocher (1960) measured 2.5 m of fault displacement in 1958 and verified probable fault-related lineaments near the mouth of Kaknau Creek mapped on lidar. Field observations also demonstrated that channel scour may have erased many fault scarps, and some scarps may be the combined effect of tectonic uplift and lateral erosion of the active stream channel.

A flight of four marine terraces at Icy Point, previously investigated by Hudson et al. (1976) and Mann (1983), provide evidence for late Quaternary differential uplift across the Fairweather fault. Mann (1983, 1986) assigned Holocene ages to the youngest two terraces (Hmt-A and -B; Plate 4) and latest Pleistocene ages to the older terraces (Pmt-C and -D). The marine platforms underlying the Icy Point terraces have not been directly dated. Ancient sea cliffs, abandoned shorelines, and isolated bedrock sea stacks punctuate the terraced peninsula at Icy Point, but similar features are absent along the eastern shoreline of Palma Bay (Plate 4). The absence of marine terraces east of the fault implies that vertical tectonic displacement drives differential uplift of Icy Point by locally outpacing relative sea-level changes since at least the most recent glaciation. Relative sea-level changes include global variations in sea level, local vertical tectonic displacements, and rapid glacial isostatic adjustments that broadly deform the Glacier Bay area, such as the rebound experienced since the mid-eighteenth century retreat of Glacier Bay ice (Larsen et al., 2005; Mann and Streveler, 2008). Tectonic uplift rates for the terraces at Icy Point are unknown because absolute ages for the terraces at Icy Point are not known. Mann (1986) estimated 4–8 mm/yr uplift rates for Pleistocene marine terraces north of Lituya Bay; however, the relationship between those terraces and the marine terraces at Icy Point is uncertain.

The geomorphic evidence for active faulting along the west bank of Kaknau Creek and the vertical deformation recorded by stream and marine terraces at Icy Point are consistent with right-lateral contractional deformation in a restraining bend where the Fairweather fault steps offshore (Brothers et al., 2020). Fault scarps along the west bank of Kaknau Creek record both vertical and strike-slip displacement on the inland side of the uplifted Icy Point

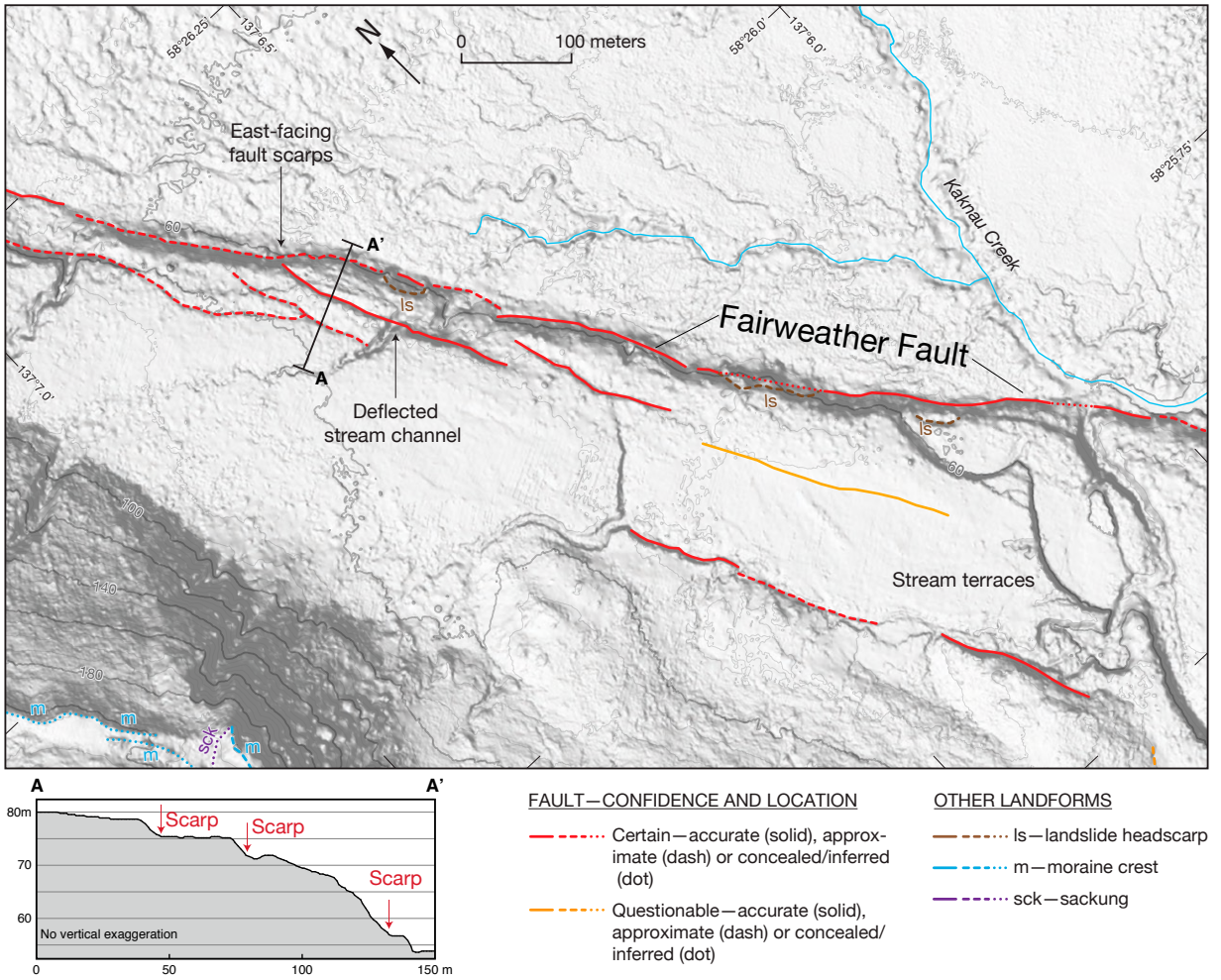

Figure 9. Map of active fault traces and other landforms revealed by light detection and ranging (lidar) along the southwest margin of Kaknau Creek at Icy Point. Location of map shown on Plate 4. Tectonic lineaments include northeast-facing scarps, offset stream channels, landslide headscarps (ls), linear valleys, and slope breaks. Other landforms indicated by colored lines denote prominent (solid), clear (dash), and subtle (dot) geomorphic expression. For example, the lower left (west) corner of the map shows recessional moraines (m) on the highest Pleistocene marine terrace and evidence for ridgetop spreading (sck). Contour interval is 5 m.

peninsula. Evidence for internal deformation of the Icy Point marine terraces include northwest-trending scarps with south-side-up deformation on terrace Pmt-C and north-side-up deformation on terrace Hmt-B (Plate 4). Additional evidence includes a reverse fault, the Finger Glacier fault, which was first observed by Hudson et al. (1976) and offsets Holocene stream and marine terraces (Hdt and Hmt-B; Plate 4) where the southern outflow stream of Finger Glacier reaches the Gulf of Alaska coast. The Finger Glacier fault warps Pleistocene and Holocene terraces and tilts these surfaces southward. From these observations, we infer that the uplift of Icy Point is accommodated by reverse faults, including the Lituya Bay–Icy Point fault mapped directly offshore (Plafker, 1967; MacKevett et al., 1971; Risley et al., 1992) (Fig. 2), and oblique-slip faults such as the main trace of the Fairweather fault at this latitude, which slips both vertically and horizontally. This system of reverse and oblique-slip faults deforming Icy Point suggests strain partitioning within a "positive flower structure" (Bruhn et al., 2004; Pavlis et al., 2004) along the eastern edge of the Yakutat block.

PALEOSEISMIC TRENCHING AT THE TOCHER FAN SITE

Approach and Methods

We used hand tools to excavate trenches and exploratory test pits across two subparallel northeast-facing scarps along the western margin of Tocher fan (Figs. 5 and 10). Trench A was ~1 m wide, <1 m deep, and extended orthogonally 4.5 m across the base of a scarp trending 305° and onto the adjacent Tocher fan surface. We present three exposures for trench A, the south and north wall (Fig. 11), and a second exposure of the north wall produced by widening the trench by ~10 cm (Fig. S9 [footnote 2]). We used a 2.5-cm-diameter gouge corer to investigate the stratigraphy in the distal part of Tocher fan and adjacent to the trench. To reveal additional exposures of the fault, we dug two smaller ~1 m^3 exploratory test pits, B and C, 1–2 m directly north and south, respectively, of the central part of trench A (Figs. 10 and 11). On a second scarp, trending 315°, upslope and subparallel to the scarp crossed by trench A, we dug trench D (Fig. 12). Trench D is located ~70 m northwest of trench A across a ~2-m-high, northeast-facing scarp that abuts a linear swale draining to Tocher fan. Trench D measured <1 m wide by 3.5 m long by ~1–3 m deep.

We cleaned the walls and marked structural and stratigraphic features using colored nails in both trenches. We constructed photomosaics (0.5 mm/pixel resolution) of the trench walls from photographs taken with a 10–22 mm lens and digital SLR camera and assembled using Agisoft Photoscan software following the methods of Reitman et al. (2015). We prepared field logs of trench exposures by mapping each wall on clear acetate film overlying photomosaics printed with a portable printer. Field photographs and sketches of test pits B and C, dug to confirm fault continuity, appear in Figures S10 and S11 (footnote 2).

Geochronological estimates of material sampled in trenches and sediment cores at Tocher fan come from accelerator mass spectrometry (AMS) ^{14}C dating methods. We collected 16 organic samples for ^{14}C dating including detrital (e.g., conifer needles, wood, and seeds) and in-growth-position (e.g., moss) plant macrofossils. ^{14}C analyses were carried out at the National Ocean Sciences Accelerator Mass Spectrometry (NOSAMS) facility in Woods Hole, Massachusetts, USA. We report calibrated ^{14}C ages in years before 1950 CE (Table 1).

To estimate times of past earthquakes recorded in the trenches, we constructed Bayesian Sequence models using OxCal (Bronk Ramsey, 2009). We follow the modeling approaches similar to those applied in other studies of active strike-slip and normal faults (e.g., Lienkaemper and Bronk Ramsey, 2009; Scharer et al., 2014; DuRoss et al., 2018). Bayesian models constructed using OxCal rely on chronological constraints, including known event times and ^{14}C dates, to compute probabilistic estimates of earthquake timing. Earthquake timing estimates are reported as the mean, 2-sigma uncertainty, and 95% confidence age ranges of the computed probability density function (PDF) in calibrated years before 1950 CE (Table 3).

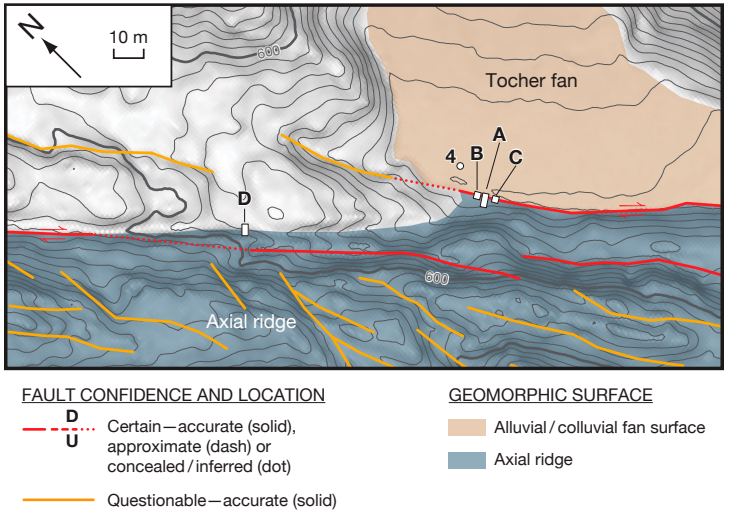

Figure 10. Map of the Tocher fan paleoseismic site showing locations of Tocher fan core 4, trenches A and D, and test pits B and C. Map located on Figure 5. Field descriptions of test pits C and D shown on Figures S10 and S11 (see text footnote 2). Contour interval is 1 m.

Stratigraphy beneath Tocher Fan

The subhorizontal, distal extent of Tocher fan fills a valley east of the Fairweather fault occupied by a pond in 1958 as shown in Figure 6A (Tocher, 1960). Our investigation of the fan includes descriptions of interbedded gravel, sand, and silt in 18 gouge cores (Fig. 5) pushed to depths up to 3.4 m below the

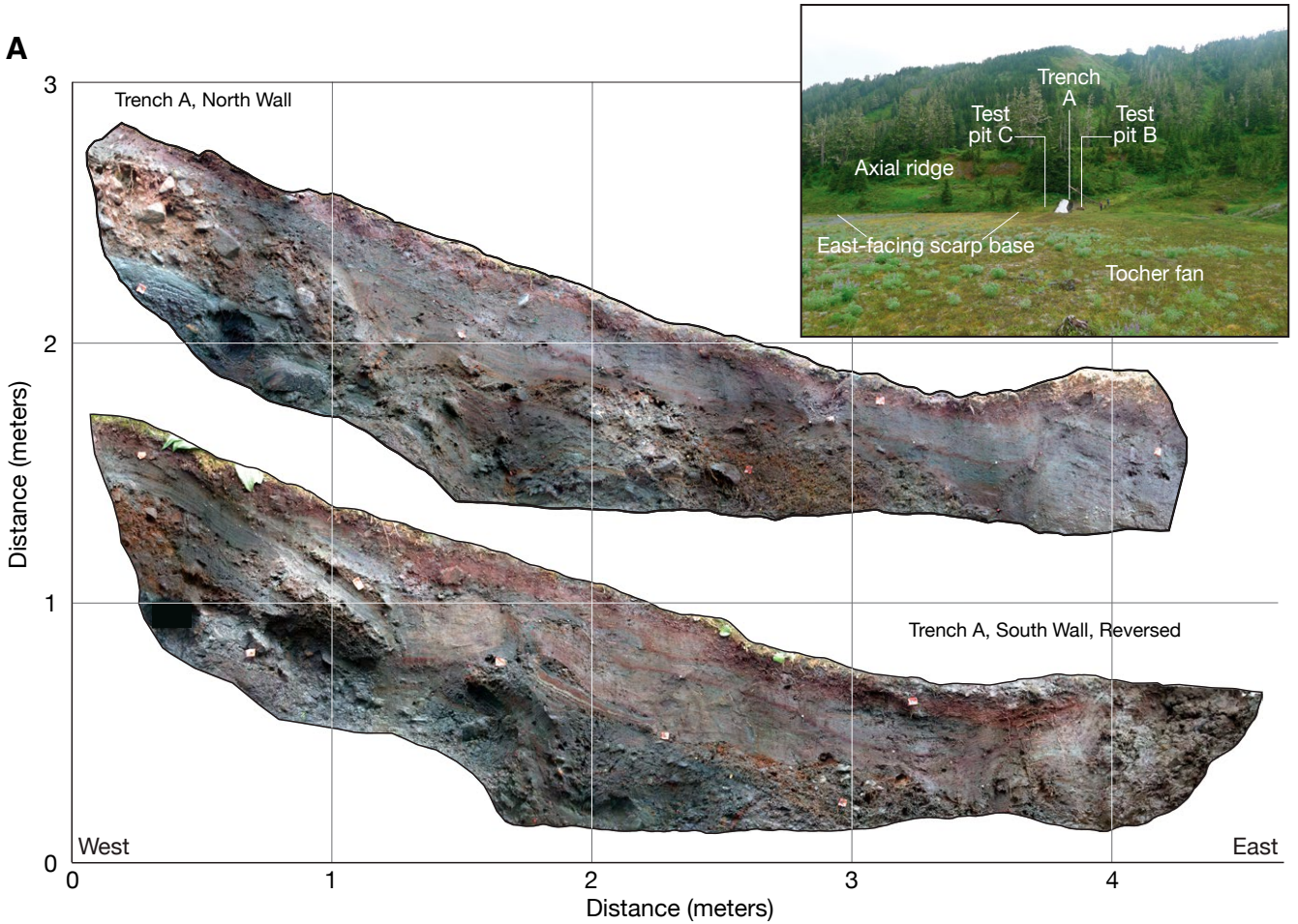

Figure 11. (A) Uninterpreted photomosaics of the north (top) and south (bottom) walls of trench A at the Tocher fan site along the Fairweather fault. The south wall is shown as a reversed image for comparison with the north wall. Figure S9 (see text footnote 2) shows a second exposure of the north wall. Inset photo, view to the west looking toward the axial ridge, shows the locations of trench A and test pits B and C. (*Continued on following page.*)

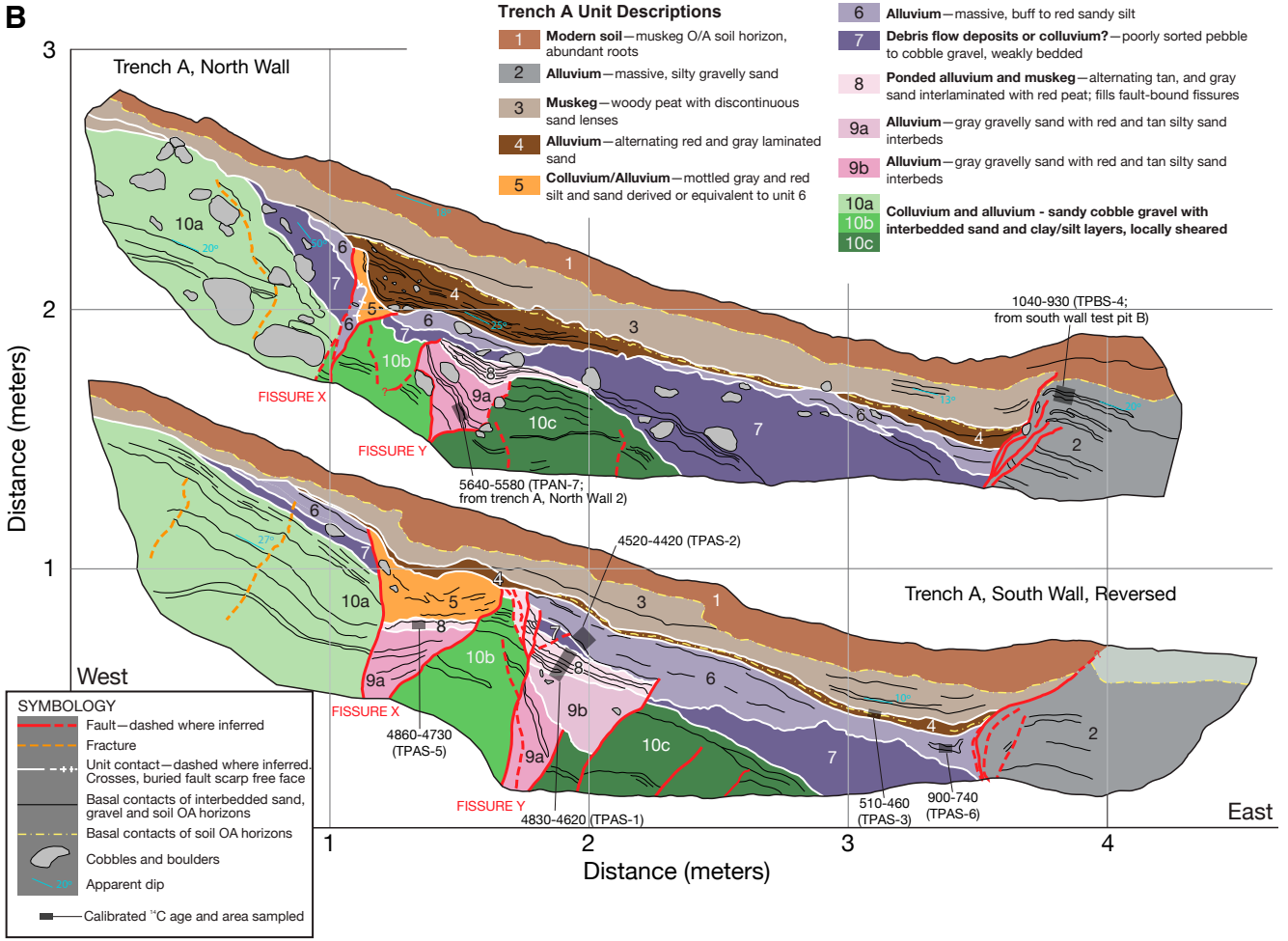

Figure 11 (*continued*). (B) Stratigraphic and structural relations logged in the north (top) and south (bottom) walls of trench A. Dark-gray areas mark locations of detrital organic samples submitted for radiocarbon dating. Calibrated age ranges (95% confidence intervals) are shown in years before 1950 CE.

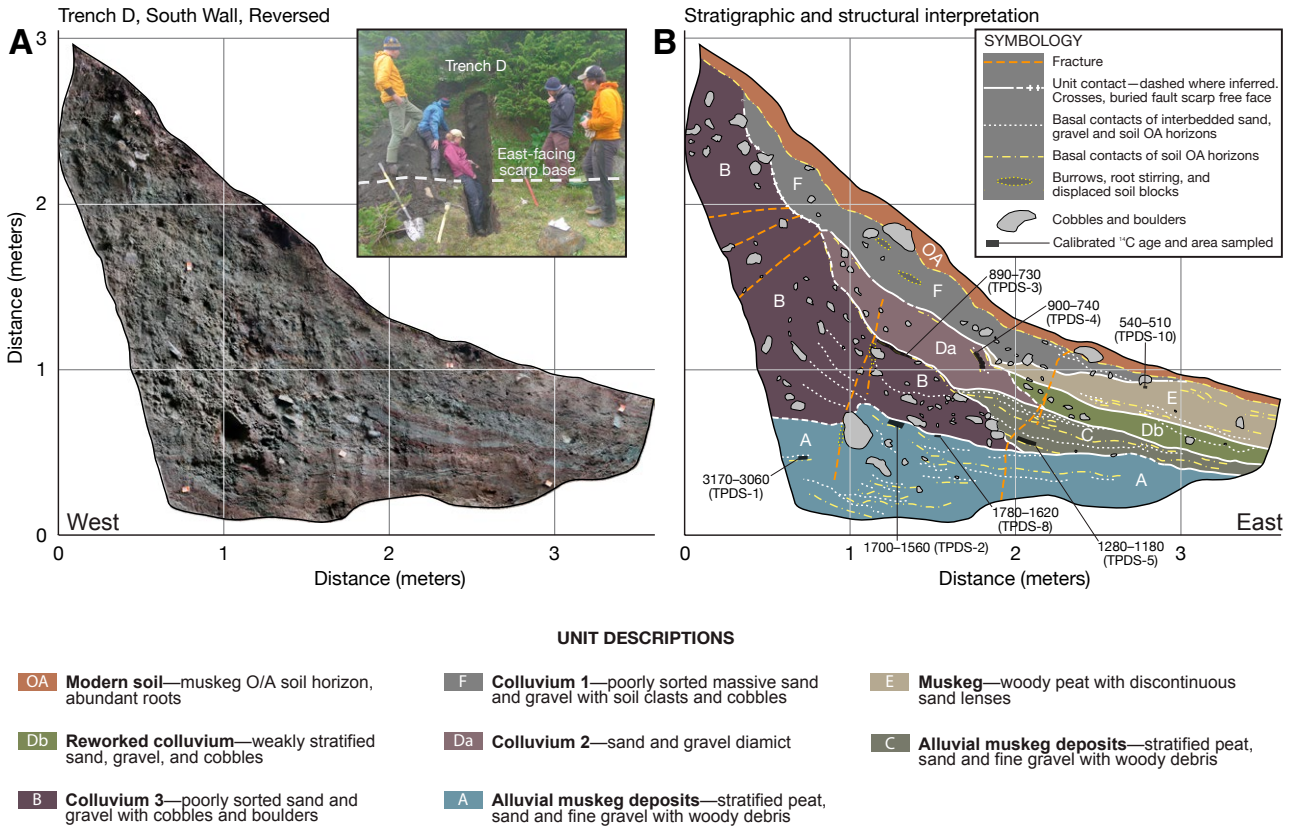

Figure 12. (A) Uninterpreted photomosaic of the south wall of trench D along the Fairweather fault. The south wall is shown as a reversed image. Inset photo of trench looking west. (B) Stratigraphic and structural relations logged in the south wall of trench D. Dark-gray areas mark locations of detrital organic samples submitted for radiocarbon dating. Calibrated age ranges (95% confidence intervals) are shown in years before 1950 CE. Brief descriptions of stratigraphic units are below trench images.

surface. The deepest cores show finely laminated silt consistent with deposition in a quiet lake or pond; other cores contain channel sand and gravel with properties similar to sediment in the modern creek channel along the western margin of the fan. Most cores hit refusal on a hard substrate ~1.3–2.5 m below the surface; two cores expose laminated fine sand and silt >3 m thick. Many cores encountered organic silt, forest soil, or peat near their bases. In one core, at a depth of 1.07 m (core 4 in Fig. 10), we sampled a 0.14-m-thick peat bed sandwiched between laminated fine sand and silt and pea-sized gravel. Calibrated ^{14}C ages of growth position moss and detrital herbaceous seeds from the upper 1 cm of the peat bed date to 1660–1950 CE (Table 3). Stratigraphic relationships inferred from these cores imply that, over a period of decades to centuries, the alluvial deposits of Tocher fan filled an ephemeral pond impounded by northeast-facing fault scarps. However, we did not detect any effects of past earthquakes in the fan stratigraphy, including 1958, that may have modulated alluvial deposition as a result of surface fault rupture.

Stratigraphic Relations in Trench A

Trench A was excavated at the base of the northeast-facing slope of the axial ridge, just uphill from a stream coursing along the western margin of Tocher fan (Figs. 5 and 10). The walls of trench A expose deposits representative

of hillslope, fan margin, and linear swale settings in a series of interbedded and faulted colluvial, alluvial, and muskeg (peat-forming wetland) deposits (Fig. 11). The oldest deposits (unit 10) consist of poorly sorted cobble gravel interbedded with laminated sand and clayey-silt layers, which we interpret as colluvium and avalanche-related deposits interbedded with meltwater silt and clay. The finer-grained layers are gently warped but show an overall dip of ~20°–25° east, slightly steeper than the current hillslope gradient. Above unit 10 is a downslope-thickening gravelly colluvial or debris flow deposit (unit 7). Colluvial units alternate with slope-parallel alluvium (units 8, 6, 4, and 3), which are broadly composed of silty and gravelly sand interbedded with reddish-brown organic-silt layers interpreted to be muskeg. Unit 5 is a massive silty sand that is interpreted to be reworked from unit 6, and in some exposures, appears to be strongly deformed. An angular unconformity occurs between the colluvial deposits and overlying alluvium at the west end of the trench (e.g., unit 3/7 contact), but these units are conformable to the east (e.g., unit 6/7 contact), indicating variable deformation and stratigraphic onlapping relationships along the trench. Unit 2 is present only on the far eastern end of the trench and is composed of laminated alluvium with muskeg interbeds, similar to the bedding observed in sediment cores obtained along the margin of Tocher fan. Unit 1 is the modern soil.

Unit 9 consists of interbedded gravelly sand with rare cobbles that fine upward to alternating gray and red silty-sand layers with diffuse contacts. Unit 9 is present only within fault-bound blocks; so its depositional source is uncertain. We consider two explanations for the origin of unit 9: first, unit 9 may represent locally sourced fissure fill. This interpretation is supported by our observations of fine-grained, bedded stratigraphy similar to deposits in exploratory cores in a fracture located southeast and above the trench on the axial ridge. Second, unit 9 may represent distal fan or linear swale deposits. How the fan or swale deposits would be restricted to fault-bound blocks surrounded by unit 10, however, is not clear. We favor the first interpretation because the absence of unit 9 outside of the fault zone suggests its distribution was limited.

Evidence for Faulting and Deformation in Trench A

Faulting in trench A is concentrated in two main zones, a complex of fissures and faulting in the center of the trench and a narrow fault zone in the east (Fig. 11). The fissure complex contains nested faulting and post-deformation fill units that are in turn faulted and tilted by subsequent event(s). Within the complex, we focus on two distinct fissure structures, identified as fissures X and Y. Both fissures are bounded by faults that cut through unit 10, and both contain unit 9, although not in all exposures. Each fissure is capped by a broad, trough-shaped unit of fine-grained alluvium (units 8 and 4). Crosscutting relationships differentiate between the relative timing of two events that formed the fissures, although some exposures provide evidence that more recent earthquakes produced additional separation along preexisting faults that formed during earlier earthquakes.

TABLE 3. SUMMARY OF AGE ESTIMATES FROM BAYESIAN AGE MODEL FOR EARTHQUAKES IN TRENCH A AND SLOPE FAILURES IN TRENCH D AT TOCHER FAN SITE

	From	To	%	μ	σ	*m*
Trench A earthquake chronology						
Event A1	470	Present	95.4	241	144	241
Event A2	810	480	95.4	641	93	639
Event A3	5590	4850	95.4	5214	224	5215
Trench D slope failure chronology						
Events D1 and D2	510	Present	95.4	259	154	259
Event D3	760	530	95.4	646	70	645
Event D4	1630	1210	95.4	1419	118	1418

Note: Modeled age ranges reported in calibrated years before 1950 (Present), rounded to nearest decade, and calculated using OxCal (version 4.3, Bronk Ramsey [2009]; 95% probability distribution at 2σ) with the IntCal13 dataset of Reimer et al. (2013). OxCal model code included in Tables S4 and S5 (see text footnote 2).

Fissure Y provides evidence for the earliest recorded earthquake in trench A, denoted as event A3. The evidence is based on faulting that juxtaposes units 9 and 10, followed by deposition of unit 8 into a small depression over the fault zone (Fig. 11). The geometry of fissure Y varies in each of three exposures (south wall and two exposures of the north wall; Figs. 11 and S9 [footnote 2]), because locally, the fissure margins are overprinted by later faulting. The best stratigraphic evidence for the earthquake comes from the eastern edge of fissure Y on the north wall, where the lower layers of unit 8 thicken into the center of the fissure and the upper layers overlap the faulting and extend for 50 cm to the east, suggesting a swale or open fissure that was progressively filled and then overlapped by unit 8. Unit 7 is not cut by faulting here, whereas the relationship of unit 8 to the fissure Y fault is more complex on the west margin of the fissure. There, the north wall exposures reveal a disconformable contact between units 8 and 7, suggesting unit 8 was either eroded or pinched out along the western fault margin. On the south wall of trench A, both margins of fissure Y appear repeatedly deformed: the eastern fault places unit 8 in fault contact with unit 6, and the western edge splays upward with the highest fault terminations truncated by unit 4, indicating evidence for earthquake(s) after deposition of unit 6. Stronger evidence for an earthquake between units 6 and 4 is provided by fissure X, so we discuss this event in greater detail in a subsequent paragraph. In either case, the west side of fissure Y does not provide the clear stratigraphic constraints preserved on the east side.

The formation of fissure Y during paleoearthquake A3 is broadly constrained by ages from detrital wood dated in unit 9 (5640–5580 cal. yr B.P.) and two samples from unit 8 (4860–4730 and 4830–4620 cal. yr B.P.); we found no dateable material in unit 10. The age of fissure Y depends on the interpreted source of unit 9, which could be reworked material from unit 10 or post-earthquake fill. In either case, the youngest age of unit 8, which caps the fissure, provides a minimum age and indicates that event A3 occurred before ca. 4620 cal. yr B.P.

Fissure X records evidence for at least two earthquakes. Units in the lower portion of fissure X on the second north wall exposure (Fig. S9) and the south wall (Fig. 11) appear equivalent to units 8 and 9, suggesting fissure X first formed at the same time as fissure Y, during event A3. Subsequent deformation of fissure X records an earthquake, event A2, when unit 6 was at the ground surface. In all walls, faulting on the west side of fissure X cuts through unit 6 and is overlain by unit 5, a chaotic deposit that is scarp-derived colluvium from unit 6 or represents sediment that is equivalent to unit 6 and has been sheared and deformed. Unit 4 is not faulted and thus postdates formation of fissure X. On both north wall exposures, unit 4 appears to fill a broad depression, thinning gradually to the east. We interpret the shape of unit 4 to reflect infilling above fissure X (at meter 1.2) and an associated broader depression (extending to meter 2.2) likely produced by distributed warping of the ground surface. On the west side of fissure X, units 6 and 7 are rotated 55°, suggesting the fault zone may extend to a weak fracture in unit 10a at meter 0.7. Overall, the associated deformation suggests that relative uplift on the west side of the fault (the axial ridge) occurred during event A2. Deposition of unit 6 at 900–735 cal. yr B.P. provides a maximum age constraint for event A2; unit 4 at 510–465 cal. yr B.P. provides a minimum constraint.

The most recent evidence of faulting in trench A, event A1, is manifested in the west-dipping fault on the east end of trenches A and B; this fault cuts through unit 1 and juxtaposes units 3, 4, and 6 against unit 2. Although the units on either side of the fault are texturally similar, no beds can be correlated between these units, suggesting substantial lateral displacement has occurred on this structure. This fault was also exposed in test pit B (Fig. S10 [footnote 2]), which was excavated just north of trench A (inset on Fig. 11). It shows stratigraphic and structural relations similar to the east end of trench A, although unit 7 appears to be lifted structurally higher, because its base is within ~40 cm of the surface and is cut by the fault. The fault forms the west side of a fault-parallel, 25-cm-high, 2-m-wide by 5-m-long, low hump at the base of the slope. Within the hump, unit 2 dips ~20° to the east, and unit 1 thickens toward the east. The fault steepens with depth and locally flattens upward; in test pit B, for example, the fault is layer parallel for short sections (Fig. S10). Unfortunately, high groundwater prevented deeper excavations to further investigate the geometry of the faulting and associated growth of the low hump.

The juxtaposition of younger unit 4 (ca. 500 cal. yr B.P.) against older unit 2 (1040–930 cal. yr B.P.) supports southward lateral translation of alluvium from the linear swale (or distal fan deposits) along the east side of the fault. Radiocarbon dating of the timing of event A1 deformation is limited only by the age of unit 4 and is thus constrained to a maximum of 510–460 cal. yr B.P. Unit 1 is the youngest deposit faulted during earthquake A1, indicating the deformation is recent and likely represents the 1958 earthquake.

Apart from faulting, in trench A, we examined folded and tilted strata that provide additional evidence for paleoearthquakes. The eastward tilt of fine-grained beds in trench A indicates wider-scale ground deformation at Tocher fan and suggests relative uplift to the west, perhaps along the axial ridge. The ~20° to 30° eastward tilt of clay and/or silt interbeds in units 10a and 10b is not likely the original depositional orientation given the grain size and planar contacts of the interbeds themselves. Similarly, fine-grained interbeds in other units tilt 20° to 25° east (see for example, interbeds in units 4 and 8). Because these units do not thicken to the east, we interpret that they have been rotated after deposition. In contrast, although units 1 and 3 dip only ~18° to the east, they thicken slightly toward the base of the slope as well, particularly on the south wall. Units 1, 3, and 4 are folded into a narrow syncline at the base of the slope (meters 3–3.7). Taken together, the eastward tilt of planar fine-grained interbeds suggests tilting has occurred since deposition. Back-rotating the entire trench by ~10° to 13° would preserve a minor hillslope component and return interbeds in unit 3 (meter 3.3) to horizontal. Local up-to-the west motion is also suggested by steeper rotations within discrete fault blocks, such as the angular unconformity between units 6 and 7 and unit 3 west of Fissure X (meter 0.9). Apart from that example and without discrete growth strata packages (i.e., units thickening to the east), we cannot distinguish if the broader tilting only occurred during the events presented above (A3, A2, and A1) or in separate earthquakes.

Stratigraphic Relations in Trench D

Trench D cuts into a ~2-m-high, northeast-facing scarp and a linear swale that parallels the northeast flank of the axial ridge, ~70 m northwest of trench A (Fig. 10). Stratigraphic units exposed in trench D consist of three east-dipping colluvial packages (units B, Da, and F; Fig. 12) that bury unit A, the oldest alluvial unit in the trench. Unit A consists of interbedded brown peat, fine-to-coarse gray sand, and gravel forming wavy layers 2–10 cm thick with sharp lower contacts. The colluvial units postdate unit A and are each interfingered with peat-forming muskeg deposited in the linear swale (units C, Db, and E; Fig. 12).

Units B and C form the oldest colluvial-peat package. Poorly sorted sand and gravel of unit B unconformably overlie unit A alluvium. Unit B, a wedge-shaped colluvial deposit, is clast-supported, including cobbles and boulders up to 0.2 m long. In the basal part of unit B, interbedded sand and gravel form an east-dipping, slope-parallel clast fabric. The triangular toe of unit B is buried by unit C, a package of interbedded fine-to-coarse sediment similar in texture to unit A and peat with abundant detrital woody debris. Unit C tapers to the west, where it buttresses unit B, and tapers gently to the east, where it conformably overlies unit A.

Units Da and Db form a colluvial-peat package that overlies units B and C. Unit Da is a sand and gravel diamict that tapers eastward and grades downslope into unit Db. Unit Da is similar in texture and sorting to unit B but is generally massive and lacks any slope-parallel fabric. A discontinuous and steeply inclined peat layer in Da may be eroded from unit B. Alluvial processes in the swale reworked the colluvium of unit Da to form Db.

The uppermost colluvium-peat package includes units F and E, which overlie units B, Da, and Db. Peat beds in unit E are up to 3 cm thick and are

interrupted by discontinuous lenses of fine sand and silt (up to 3 cm thick). Unit F is an east-dipping wedge of colluvium that consists of poorly sorted sand and gravel. The unit is similar in texture to units B and Da and has a steep (slope-parallel) clast fabric, locally including tabular soil blocks up to 22 cm long. Unit F unconformably overlies the steep contact between units B and Da but has a mostly conformable relationship with Da and E downslope. Unit F overlies alluvial unit E, which consists of interbedded peat, silt, and sand, and is similar to units A, C, Db, and E. Unit OA is a deep reddish-brown peaty muskeg soil that mantles the scarp.

Evidence for Cracking and Colluviation in Trench D

Photographs taken following the 1958 earthquake show surface rupture in the vicinity of trench D as vertical scarps and associated slope failures (Fig. S4 [footnote 2]). Although we observed no discrete faults in trench D, we interpret that the trench records colluvial sedimentation related to coseismic deformation occurring along the axial ridge west of the trench extent. In this scenario, the colluvial packages with slope-parallel clast fabric and interbedded peat and alluvium, together with fractures and crosscutting relations, suggest that two to four earthquakes are recorded in the trench. However, there is no primary fault evidence in trench D, and thus, we cannot rule out a gravitational (e.g., landslide) and/or shaking-related origin for the deposits and crosscutting relations.

No discrete faults displace units in trench D. However, several fractures (orange dashed lines; Fig. 12) crosscut colluvial units and suggest the sediments responded to nearby deformation or earthquake shaking. The fractures do not show evidence for lateral or vertical displacement. The most prominent fractures dip west and appear in unit B as changes in color and fabric. Two additional fractures to the east of the west-dipping fractures continue upward into units Da and possibly F. The easternmost fracture could have extended to the surface but could not be confidently mapped in soil unit OA.

Stratigraphic and structural evidence from trench D suggests several episodes of surface disturbance, possibly related to earthquake shaking and surface rupture. Alluvium in unit A was at the surface as late as 1780–1560 cal. yr B.P. (Table 1). A surface disturbance (surface rupture or slope failure) resulted in deposition of poorly sorted colluvial sediment (unit B) unconformably over unit A. Alluvial deposits and peat in unit C bury the toe of unit B and date to 1280–1180 cal. yr B.P.. Detrital twigs in unit B suggest soil processes at the surface as late as 890–730 cal. yr B.P. An additional colluvial-peat package (units Da and Db) postdates units B and C, but peat from within unit Da (900–740 cal. yr B.P.) yields similar age to that from soil developed in unit B (890–730 cal. yr B.P.; Table 1). Unit D possibly represents (1) colluvial sediment from a younger surface disturbance or surface rupture with organic matter recycled from unit B, or (2) the gravitational failure and/or erosion of the unit B colluvial wedge. Peat and alluvial deposition (unit E) continued at the base of the scarp as late as ca. 540–510 cal. yr B.P. West-dipping fractures in unit B, erosion or failure of the scarp, and deposition of colluvial unit F on unit E likely signal earthquake shaking and possibly surface rupture near the trench. Weak evidence of a younger, additional earthquake is from a single fracture within unit F. This fracture formed after deposition of unit E dated to 540–510 cal. yr B.P.

Interpretation of Colluvial Wedges and Fractures in Trench D

The oldest wedge-shaped colluvial package, unit B, overlies mixed alluvial and muskeg deposits of unit A and records the oldest surface disturbance (event D4) evident in trench D. We infer unit B was derived from material eroded from a scarp west of the trench; the scarp may have been produced by a fault or faults not observed in the trench. Alternatively, unit B may reflect slope failure unrelated to faulting. Maximum limiting ages for deposition of unit B (e.g., 1700–1560 cal. yr B.P.) come from unit A; a minimum limiting age of 1280–1180 cal. yr B.P. comes from unit C (Table 1). Detrital twigs in soil developed in unit B (sample TPDS-3, 890–730 cal. yr B.P.) postdate deposition of both units B and C.

A wedge-shaped colluvial package, unit Da, records scarp erosion during event D3. Unit Da overlies both units B and C; its downslope facies (unit Db) consists of stratified sand and gravel deposited in an environment similar to the present swale. Bracketing ages from twigs in soil marking the former surface of unit B (890–730 cal. yr B.P.) and conifer needles in unit E (Table 1) provide maximum and minimum limits on the time unit Da formed. A fragmented peat layer in unit Da, probably eroded from unit B, yielded an age of 900–740 cal. yr B.P., nearly identical to the age of soil developed in unit B. This peat, likely eroded from unit B, provides an additional maximum constraint on the age of unit Da deposition. Because no fractures terminate at the Da/B contact and considering the limited lateral extent of unit Da, we cannot rule out a gravitational, non-earthquake-induced origin for this event.

Scarp erosion associated with event D2 is evidenced by unit F colluvium that buries older colluvial and muskeg deposits in the scarp, including unit E. White crosses in Figure 12 mark a buried scarp associated with shallow, west-dipping fractures overlain by unit F; these fractures imply an earthquake origin for this event. Event D2 occurred after deposition of woody peat and sand lenses in unit E. A fracture that cuts units A–F, but not the modern soil horizon (unit OA), implies that deposition of colluvial unit F in trench D was not related to the 1958 earthquake. An age of 540–510 cal. yr B.P. from unit E (Table 1) provides a maximum age constraint for event D2.

Weak evidence for the 1958 earthquake, event D1 in trench D, comes from a single buried fracture that extends through units A–F. However, the trench exposed no recent colluvial deposit younger than unit F and, unlike in the south wall of trench A, we did not observe deformation of the modern soil (unit OA). Event D1 postdates unit E dated to 540–510 cal. yr B.P. (Table 1) and the penultimate event recorded by unit F. Tocher's (1960) observations of fractures aligned with the scarp allow the possibility that the 1958 earthquake produced the fracture.

DISCUSSION

Event Chronology Inferred from OxCal Modeling

We estimate the 95% confidence age ranges, using OxCal (Bronk Ramsey, 2009), for the times of events interpreted from stratigraphic and structural relations in the Tocher fan trenches (Table 3). OxCal model codes are included in Supplemental Material 2 (Tables S4 and S5 [footnote 2]). The graphic representation of the age models, shown in Figure 13, depicts event ages as probability density functions (PDFs) in color constrained by layer ages in gray.

The age model for trench A computes age ranges for three earthquakes in the past 5600 years (Fig. 13 and Table 3). We infer that the age of unit 9 predates formation of Fissure Y and estimate the age of earthquake A3 to between 5590 and 4850 cal. yr B.P. Earthquake A2 spans 810–480 cal. yr B.P. Finally, although the chronological constraints are poor, evidence for faulting in the modern soil suggests event A1 is the 1958 earthquake. Because only maximum age constraints are available from unit 4, the modeled PDF for event A1 spans the past 470 years. Finally, the chronology for trench A features a notable 3900-year-long gap in the record of deposition between earthquakes A3 and A2.

A second, independent age model for trench D computes age ranges for four scarp disturbances in the past ~3200 years (Fig. 13 and Table 3). The oldest colluvial deposit records event D4, which occurred between 1620 and 1210 cal. yr B.P.; event D3 occurred between 760 and 530 cal. yr B.P.; and the youngest colluvial deposit (D2) formed in the past 510 cal. yr B.P., but prior to 1958. A single fracture that extends up to the modern soil suggests shaking related to 1958 at the site (event D1). Sparse minimum-limiting constraints on the time of event D2 result in a modeled PDF that entirely overlaps the PDF for earthquake A1 in trench A. However, because event A1 deforms the modern soil, while event D2 does not, we interpret that event D2 occurred before event A1. The PDF for event D3 is entirely encompassed by the PDF for event A2, which implies close correlation in time. The age ranges for the oldest events in trench D and trench A are separated by ~3900 years.

Considering the chronological data, both trenches preserve evidence for up to six earthquakes in the past 5600 years. Trench D records three events that formed colluvial deposits (Fig. 13) and a fourth event—possibly the 1958 earthquake—that caused cracking near the present ground surface. If the colluvial deposits in trench D record slope failures not triggered by seismic shaking or surface fault rupture, then the two trenches together record only three earthquakes in the past 5600 years. However, if colluvial deposits in trench D reflect response to earthquakes, then taken together, both trenches may record a total of six events in the past 5600 years. A chronology of six earthquakes assumes near-surface cracking in trench D formed during the 1958 earthquake, and events A2 and D3, despite their overlapping ages, are different events recorded in separate trenches.

The Tocher fan trenches allow as many as four and as few as two earthquakes in the past 810 years. In this interval, trench A records two surface-fault

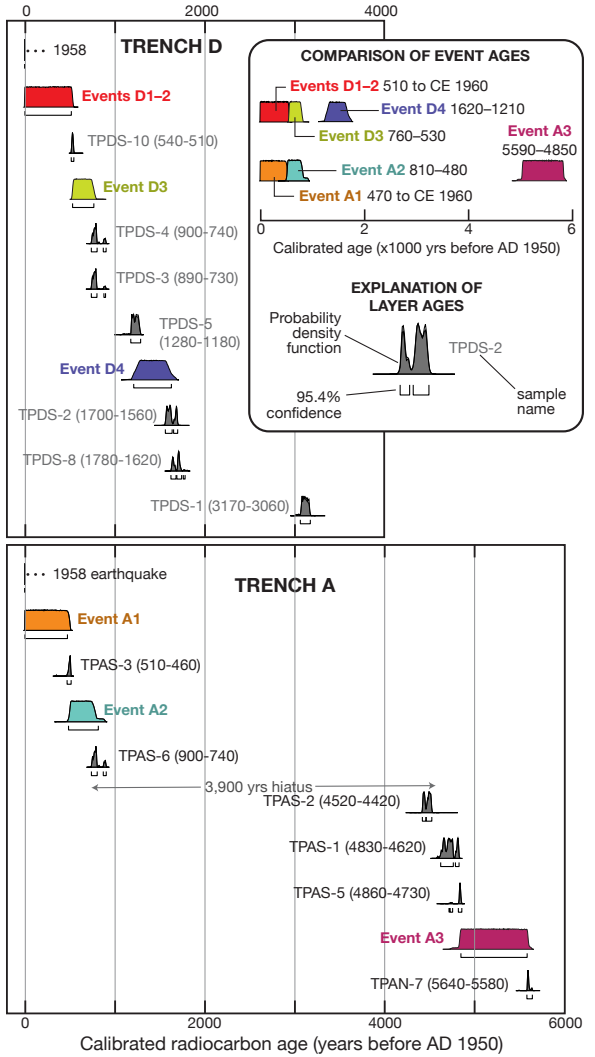

Figure 13. OxCal Bayesian age models for trenches A and D at the Tocher fan site depicting probability density functions (PDFs) for ^{14}C dates used to constrain model age ranges for disturbances in trench D (top) and faulting in trench A (bottom). Colored PDFs show model age ranges (in years before 1950 CE) that span the 95% confidence interval (Table 3). Gray PDFs show layer ages (Table 1) used to constrain model ages. The year of the 1958 earthquake, shown at the top of both models, also is used as a model constraint. We construct age models with OxCal version 4.3.2 (Bronk Ramsey, 2009) and the IntCal13 atmospheric curve (Reimer et al., 2013); model code included in Tables S4 and S5 (see text footnote 2). Inset shows overlaps among events D1–D3 and A1–A2. Sample IDs (e.g., TPDS-10), assigned in the field, identify the Tocher Pond locality (TP), trench D or A, the south (S) or north (N) trench wall, and the sample number.

rupturing events: the 1958 earthquake (event A1) and event A2 at 810–480 cal. yr B.P. (Table 3). Trench D contains evidence for two colluvial wedges (events D2 and D3) and cracking in event D1 in the past 760 years. If the colluvial deposits in trench D reflect earthquakes, then the Tocher fan site may record as many as four earthquakes in the past 810 years (D1 = A1, D2, D3, and A2). The overlapping PDFs for event A2 and D3 (Fig. 13) allow, but do not require, that at least one of the colluvial wedges in trench D formed in response to a large earthquake. Faulting of the modern soil in event A1 and a fracture in trench D suggests the 1958 earthquake deformed both trench sites.

An Incomplete History of Holocene Faulting at the Tocher Fan Site

Exploratory trenches across active fault scarps at the Tocher fan site suggest that predecessors of the strong 1958 M_w 7.8 Fairweather earthquake ruptured a number of different fault strands evident in the landscape (Fig. 5 and Plate 3). We excavated paleoseismic trenches across two scarps that delineate the eastern margin of an axial ridge, which was pervasively deformed during the 1958 Fairweather earthquake (Tocher, 1960). However, compared to published earthquake recurrence intervals (60–110 years) for the Fairweather fault (Plafker et al., 1978), the Tocher fan trenches likely preserve evidence for only a small fraction of the large earthquakes in the past 5600 years. Published slip rates for the Fairweather fault (Plafker et al., 1978; Brothers et al., 2020; Elliott and Freymueller, 2020) vary from 46 to 58 mm/yr and imply average recurrence intervals of 60–140 years for M_w >7 earthquakes with 3.5 m (average) to 6.5 m (maximum) slip per event (Table 4). Yet the two Tocher fan trenches contain evidence for ≤15% of the 40–93 events expected assuming the recurrence estimates are accurate. The record of two to four earthquakes in the past 810 years implies an earthquake recurrence interval ≥270 years. However, the younger two to four event record would require an average displacement of >10 m per earthquake to maintain the Holocene slip rate, which suggests that even the most recent ~1600 years of the Tocher fan record lacks evidence for ~50% of possible earthquakes.

We conclude that the Tocher fan trenches record an incomplete history of Fairweather fault earthquakes. We chose the trench sites because they appeared to provide locations where active deposition from the linear swale and Tocher fan would capture faulting along the margin of the ridge, as opposed to trenches on the axial ridge, where sedimentation rates would be low. Given the limited evidence of rupture in the trenches and a long hiatus, coseismic deformation at the base of the axial ridge appears to be limited or episodic and instead may be concentrated closer to the crest of the axial ridge.

The incomplete record of surface fault rupture at the Tocher fan site may be the result of complex faulting, fault reactivation, and limited and/or coarse sedimentation. For example, evidence from trench D is based on secondary deformation (slope failure), and the faulting itself is otherwise obscured. Trench D did not expose a primary fault zone; thus, missing events in the time period represented by the colluvial and alluvial units is not surprising. In trench A, the primary problem is limited deposition. For example, in the past 900 years, the trench records only ~50 cm of section, and much of that is massive. The slow sedimentation rate makes repeated faulting, which is suggested by the complexity of the fissure margins, difficult to separate into more than a few events.

The simple geomorphic expression of active faulting between La Perouse and Finger Glaciers (Plate 3) may offer sites with greater potential for evaluating a more complete history of slip on the Fairweather fault. We map a <20-m-wide, well-defined zone of fault scarps and slope breaks in the northwestern part of this valley. This zone of deformation tapers southeast to a single 4-m-wide linear trough between a shutter ridge and the eastern flank of Middle Dome (Fig. 7). The shutter ridge juxtaposes an uphill-facing fault scarp against ponded sediment carried into the trough by debris-flow gullies and alluvial processes (profile A–A′, Fig. 7). The sediment ponded behind the shutter ridge, within the narrow fault trough, may capture a more complete record of earthquakes than at other sites. This site also offers the unique opportunity to directly refine the late Holocene slip rate of the Fairweather fault by more precisely dating the highest northeastern Finger Glacier moraine crest with modern geochronology techniques.

TABLE 4. PUBLISHED SLIP RATES AND INFERRED EARTHQUAKE RECURRENCE INTERVALS FOR THE FAIRWEATHER FAULT

Slip rate (mm/yr)	Slip deficit over 5600 yr (m)	No. of events with 3.5 m slip	No. of events with 6.5 m slip	Average recurrence interval (yr)	Source
45*	252	72	39	78–144	Elliott and Freymueller (2020)
48†	269	77	41	73–136	Plafker et al. (1978)
50†	280	80	43	70–130	Brothers et al. (2020)
57§	319	91	49	61–114	Brothers et al. (2020)
58§	325	93	50	60–112	Plafker et al. (1978)

*Block model strike-slip rate for the southern Fairweather fault, 45.4 ± 0.6 mm/yr.
†Minimum reported slip rate.
§Maximum reported slip rate.

Revised Geological Estimates of Fairweather Fault Slip Rates

Our geological estimates of Fairweather fault strike-slip rates derived from lidar-based geomorphic offset measurements and calibrated age data generally corroborate published rates that range from 45 to 58 mm/yr (Plafker et al., 1978; Brothers et al., 2020; Elliott and Freymueller, 2020). The fastest published slip rate, 58 mm/yr, reported by Plafker et al. (1978), comes from measured offset of a stream channel at Crillon fan that we reevaluate using lidar (Figs. S3 and S4 [footnote 2]). The slowest published slip rate is derived from a geodetic block model (Elliott and Freymueller, 2020), which places ~45 mm/yr of strike-slip motion on the Fairweather fault and ~4 mm/yr on the Foothills thrust fault (FT on Fig. 1). We reevaluate slip rates at two sites examined by Plafker et al. (1978) by using lidar topography and LaDiCaoz to reconstruct stream channels and moraines offset by the Fairweather fault. We use a limited data set of previously published ^{14}C dates with large uncertainties to estimate the ages of offset landforms. Because some ^{14}C dates constrain the maximum age of a landform, two of our three estimates are minimum slip rates.

Our geologic slip-rate estimates (Table 2) suggest that the southern Fairweather fault may accommodate ≥90% of the Yakutat block relative motion. Our revised estimates also permit that some horizontal motion occurs on oblique reverse faults such as the Foothills and Lituya Bay–Icy Point faults (Figs. 1 and 2). At the Crillon fan, we estimate a minimum slip rate of ≥49 mm/yr using the full range of offset measurements of the central stream channel (Table 2). The estimate is consistent with the 48–58 mm/yr estimate of Plafker et al. (1978) and slightly higher than the ~45 mm/yr strike-slip rate estimated by block models (Elliott and Freymueller, 2020). We also reevaluate slip rates by reconstructing two offset moraines of different ages along the northern margin of Finger Glacier. We use the 105–116 m offset of the older and highest moraine and an OxCal age model to estimate a broad slip rate of 26–72 mm/yr (Table 2). The mean estimate, 49 mm/yr, lies within the range of published slip-rate estimates, but large uncertainties contributed by poor constraints on the age of the moraine surround this estimate. Maximum age constraints on a younger recessional moraine and measured offset yield a minimum slip rate estimate of ≥27 mm/yr (Table 2), which is considerably slower than published rates.

Deformation Style of the Southern Fairweather Fault

Our geomorphic mapping along the southern Fairweather fault identifies evidence for right-lateral, strike-slip faulting with a component of west-side-up vertical deformation. For example, at the Crillon Lake site, prominent northeast-facing scarps imply distributed deformation on at least two west-side-up fault strands that offset late Holocene till and stream channels. In addition, measurements of fault displacement at this site following the 1958 earthquake showed a 6:1 ratio of right-lateral to vertical motion (Tocher and Miller, 1959; Tocher 1960) on a fault dipping ~80° northeast. However, Tocher (1960) emphasized that strike-slip, without detectable vertical deformation, dominated all other measurements of 1958 fault displacements in the field, which is consistent with the earthquake's strike-slip focal mechanism (Doser and Lomas, 2000).

Other geomorphic features revealed by lidar and mapped in the field indicate oblique-slip faulting consistent with transpressive deformation (e.g., Sylvester, 1988; Cunningham and Mann, 2007). The axial ridge at the Tocher fan site, for instance, resembles a pressure ridge contracting between two subparallel fault strands (Fig. 5) with strikes oblique to Yakutat block motion. The ridge is ~1100 m long and 45–90 m wide. Tocher (1960) described a continuous zone of right-lateral deformation along the northeast side of the axial ridge and chaotically oriented hummocks and open fractures, tens of meters in length, across the ridgetop (Fig. 6A). Our mapping depicts prominent fault scarps bounding the southwest and northeast sides of the axial ridge and north-trending lineaments, including linear troughs and depressions (Fig. 5). The geometry of these features suggests transpressional deformation accommodating contraction across a local restraining bend in the fault. In this model, faults along the ridge margins accommodate oblique-reverse slip, and open fractures aligned with the principal horizontal stress (approximately north-south) relieve tension as the ridge contracts. The high length-to-width ratio of the ridge indicates that the faults bounding the ridge predominantly accommodate strike-slip motion, and the overall amount of convergence across the ridge is low.

Flights of marine and stream terraces at Icy Point indicate differential tectonic uplift of a >3-km-wide block west of the Fairweather fault. Tectonic uplift east of the fault, which should produce similar terraces, is not observed (Mann and Streveler, 2008). Discrete scarps in the lidar maps reveal discontinuous faults that vertically displace the marine terraces by meters (Plate 4). For example, the Finger Glacier fault (Hudson et al., 1976), a probable reverse fault that borders the western margin of the peninsula and vertically offsets Holocene marine terraces, accommodates uplift of Icy Point. Additional contractional structures that drive uplift, including the Lituya Bay–Icy Point fault, have been mapped offshore (Plafker, 1967; Bruns, 1983; Risley et al., 1992; Brothers et al., 2020).

Taken together, our results reflect transpressional deformation along the southern Fairweather fault in the Crillon Lake–Icy Point restraining bend (Fig. 2 and Plate 1). The geomorphic lineaments and landforms we map resemble features identified along other transpressional strike-slip systems (Sylvester, 1988; Wallace, 1990; Teyssier and Tikoff, 1998; Cunningham and Mann, 2007). Our observations are consistent with marked changes in along-strike obliquity of the Fairweather–Queen Charlotte fault system north of Icy Point compared to a revised model for Yakutat block motion (Brothers et al., 2020).

Uplift of the coastal foothills between Lituya Bay and Icy Point likely reflects deformation across a transpressional zone of strike slip, with oblique-slip and reverse faults that accommodate contraction in the Crillon Lake–Icy Point restraining bend (Fig. 2 and Plate 1). Transpressive deformation also drives uplift of the Fairweather Range east of the bend but at rates three to four times slower than Pleistocene exhumation rates of Yakutat sedimentary cover present in the coastal foothills west of the bend (Lease et al., 2021). Our study raises several questions motivating further research: what additional faults, such as the Finger Glacier fault, lie west of the Fairweather fault; and do restraining-bend

fault geometries resemble a positive flower structure or reflect other kinematics? To what extent is lateral and vertical slip partitioned onto different structures within the restraining bend (e.g., Bruhn et al., 2004) and on what timescales? Does the Fairweather fault accommodate all of the lateral slip, as suggested by slip-rate estimates, or is some fraction of the horizontal motion taken up by offshore faults? Finally, do offshore faults bounding the western margin of the uplifted coastal block present previously unrecognized tsunami sources?

CONCLUSIONS

Active traces of the southern Fairweather fault evident in lidar topography and verified in the field reveal the impacts of large (M_w >7) surface-rupturing earthquakes and transpressional deformation along the boundary between the Yakutat block and North America. Fault displacement of a stream channel on the Crillon fan, measured in this study, implies a rate of strike-slip ≥49 mm/yr and corroborates published slip-rate estimates that place most of the ~53 mm/yr plate boundary motion on the Fairweather fault (Plafker et al., 1978; Brothers et al., 2020; Elliott and Freymueller, 2020). However, the slip rate we estimate from reanalysis of the northeastern Finger Glacier lateral moraines encompasses greater uncertainty inherent in ^{14}C ages and measuring fault displacement, and permits that other structures west of the Fairweather fault may accommodate an increasingly larger component of convergent plate motion toward the north like that deduced from block models constrained by satellite geodesy (Elliott and Freymueller, 2020).

As one of Earth's fastest slipping transform plate boundaries, the Fairweather fault is capable of producing large (M_w >7) earthquakes at intervals on the order of a century or less. The results of exploratory trenches across scarps at the Tocher fan site suggest that predecessors of the strong 1958 M_w 7.8 Fairweather earthquake ruptured a number of different fault strands evident in the landscape. The Tocher fan trenches preserved evidence for up to six ground-rupturing earthquakes in the past 5600 years, and two to four earthquakes in the past 810 years. The younger record implies a recurrence interval of ≥270 years for large earthquakes in the past 810 years, over two times longer than expected given the Holocene slip rate and typical earthquake displacements. Our geomorphic maps of this active fault zone indicate considerably greater structural complexity than previously recognized. The complex fault structure is consistent with transpressional deformation in a double restraining bend that activates oblique-slip and reverse faulting and drives greater rates of rock uplift in the coastal foothills west of the Fairweather fault compared to the Fairweather Range to the east.

ACKNOWLEDGMENTS

We appreciate T. Lewis and L. Sharman of Glacier Bay National Park for guidance with permitting and logistics. The pilots and staff at Ward Air provided float plane transport to Crillon Lake. J. Kearns of Fairweather Adventures safely transported our team to Icy Point. We acknowledge K. Hudnut for assistance with lidar visualizations. Reviews by Ashley Streig, Belle Philibosian, and the Associate Editor improved the manuscript. Any use of trade, firm, or product names is for descriptive purposes only and does not imply endorsement by the U.S. Government.

REFERENCES CITED

Bronk Ramsey, C., 2009, Bayesian analysis of radiocarbon dates: Radiocarbon, v. 51, p. 337–360, https://doi.org/10.1017/S0033822200033865.

Brothers, D.S., Miller, N.C., Barrie, J.V., Haeussler, P.J., Greene, H.G., Andrews, B.D., Zielke, O., Watt, J., and Dartnell, P., 2020, Plate boundary localization, slip-rates and rupture segmentation of the Queen Charlotte fault based on submarine tectonic geomorphology: Earth and Planetary Science Letters, v. 530, no. 115882, https://doi.org/10.1016/j.epsl.2019.115882.

Bruhn, R.L., Pavlis, T.L., Plafker, G., and Serpa, L., 2004, Deformation during terrane accretion in the Saint Elias orogen, Alaska: Geological Society of America Bulletin, v. 116, p. 771–787, https://doi.org/10.1130/B25182.1.

Bruns, T.B., 1983, Model for the origin of the Yakutat block, an accreting terrane in the northern Gulf of Alaska: Geology, v. 11, p. 718–721, https://doi.org/10.1130/0091-7613(1983)11<718:MFTOOT>2.0.CO;2.

Cunningham, W.D., and Mann, P., 2007, Tectonics of strike-slip restraining and releasing bends: Geological Society of London, Special Publications, v. 290, p. 1–12, https://doi.org/10.1144/SP290.1.

Doser, D.I., 2010, A reevaluation of the 1958 Fairweather, Alaska, earthquake sequence: Bulletin of the Seismological Society of America, v. 100, p. 1792–1799, https://doi.org/10.1785/0120090343.

Doser, D.I., and Lomas, R., 2000, The transition from strike-slip to oblique subduction in southeastern Alaska from seismological studies: Tectonophysics, v. 316, p. 45–65, https://doi.org/10.1016/S0040-1951(99)00254-1.

DuRoss, C.B., Bennett, S.E.K., Briggs, R.W., Personius, S.F., Gold, R.D., Reitman, N.G., Hiscock, A.I., and Mahan, S.A., 2018, Combining conflicting Bayesian models to develop paleoseismic records: An example from the Wasatch Fault Zone, Utah: Bulletin of the Seismological Society of America, v. 108, p. 3180–3201, https://doi.org/10.1785/0120170302.

Dusel-Bacon, C., 1994, Metamorphic history of Alaska, *in* Plafker, G., and Berg, H.C., eds., The Geology of Alaska: Boulder, Colorado, Geological Society of America, Geology of North America, v. G-1, p. 495–533.

Elliott, J., and Freymueller, J.T., 2020, A block model of present-day kinematics of Alaska and western Canada: Journal of Geophysical Research. Solid Earth, https://doi.org/10.1029/2019JB018378.

Fritz, H.M., Mohammed, F., and Yoo, J., 2009, Lituya Bay landslide impact generated mega-tsunami 50th anniversary: Pure and Applied Geophysics, v. 166, p. 153–175, https://doi.org/10.1007/s00024-008-0435-4.

Haddon, E.K., Amos, C.B., Zielke, O., Jayko, A.S., and Bürgmann, R., 2016, Surface slip during large Owens Valley earthquakes: Geochemistry, Geophysics, Geosystems, v. 17, p. 2239–2269, https://doi.org/10.1002/2015GC006033.

Hudson, T.L., and Plafker, G., 1982, Paleogene metamorphism of an accretionary flysch terrane, eastern Gulf of Alaska: Geological Society of America Bulletin, v. 93, p. 1280–1290, https://doi.org/10.1130/0016-7606(1982)93<1280:PMOAAF>2.0.CO;2.

Hudson, T., Plafker, G., and Rubin, M., 1976, Uplift rates of marine terrace sequences in the Gulf of Alaska, *in* Cobb, E.H., ed., The United States Geological Survey in Alaska, Accomplishments during 1975: U.S. Geological Survey Circular 733, p. 11–13.

Larsen, C.F., Motyka, R.J., Freymueller, J.T., Echelmeyer, K.A., and Ivins, E.R., 2005, Rapid viscoelastic uplift in southeast Alaska caused by post-Little Ice Age glacial retreat: Earth and Planetary Science Letters, v. 237, p. 548–560, https://doi.org/10.1016/j.epsl.2005.06.032.

Le Pichon, X., 1968, Sea-floor spreading and continental drift: Journal of Geophysical Research, v. 73, p. 3661–3697, https://doi.org/10.1029/JB073i012p03661.

Lease, R.O., Haeussler, P.J., Witter, R.C., Stockli, D.F., Bender, A.M., Kelsey, H.M., and O'Sullivan, P.B., 2021, Extreme Quaternary plate boundary exhumation and strike-slip localized along the southern Fairweather fault, Alaska: Geology, https://doi.org/10.1130/G48464.1.

Lienkaemper, J.J., and Bronk Ramsey, C., 2009, OxCal: Versatile tool for developing paleoearthquake chronologies—A Primer: Seismological Research Letters, v. 80, p. 431–434, https://doi.org/10.1785/gssrl.80.3.431.

MacKevett, E.M., Brew, D.A., Hawley, C.C., Huff, L.C., and Smith, J.G., 1971, Mineral resources of Glacier Bay National Monument, Alaska: U.S. Geological Survey Professional Paper 632, 90 p., https://doi.org/10.3133/pp632.

Mann, D.H., 1983, The Quaternary history of the Lituya glacial refugium, Alaska [Ph.D. thesis]: Seattle, Washington, University of Washington, 268 p.
Mann, D.H., 1986, Wisconsin and Holocene glaciation of southeast Alaska, *in* Hamilton, T.D., Reed, K.M., and Thorson, R.M., eds., Glaciation in Alaska: Anchorage, AK, Alaska Geological Society, p. 237–265.
Mann, D.H., and Streveler, G.P., 2008, Post-glacial relative sea level, isostasy, and glacial history in Icy Strait, Southeast Alaska, USA: Quaternary Research, v. 69, p. 201–216, https://doi.org/10.1016/j.yqres.2007.12.005.
Mann, D.H., and Ugolini, F.C., 1985, Holocene glacial history of the Lituya District, southeast Alaska: Canadian Journal of Earth Sciences, v. 22, p. 913–928, https://doi.org/10.1139/e85-095.
Marincovich, L., 1980, Miocene mollusks of the Topsy Formation, Lituya District, Gulf of Alaska Tertiary Province, Alaska: U.S. Geological Survey Professional Paper 1125C, 14 p.
Mertie, J.B., 1931, Notes on the geography and geology of Lituya Bay, Alaska: U.S. Geological Survey Bulletin 836-B, p. 117–135.
Miller, D.J., 1960, The Alaska earthquake of July 10, 1958: giant wave in Lituya Bay: Bulletin of the Seismological Society of America, v. 50, p. 253–266.
Molnar, P., and Dayem, K.E., 2010, Major intracontinental strike-slip faults and contrasts in lithospheric strength: Geosphere, v. 6, p. 444–467, https://doi.org/10.1130/GES00519.1.
Page, R., 1969, The Fairweather fault ten years after the southeast Alaska earthquake of 1958: Bulletin of the Seismological Society of America, v. 59, p. 1927–1936.
Page, R.A., 1973, The Sitka, Alaska, earthquake of 1972—An expected visitor: Reston, Virginia, U.S. Geological Survey Earthquake Information Bulletin, v. 5, p. 4–9.
Pavlis, T.L., and Sisson, V.B., 1995, Structural history of the Chugach metamorphic complex in the Tana River region, eastern Alaska: A record of Eocene ridge subduction: Geological Society of America Bulletin, v. 107, p. 1333–1355, https://doi.org/10.1130/0016-7606(1995)107<1333:SHOTCM>2.3.CO;2.
Pavlis, T.L., Picornell, C., Serpa, L., Bruhn, R.L., and Plafker, G., 2004, Tectonic processes during oblique collision: Insights from the St. Elias orogen, northern North American Cordillera: Tectonics, v. 23, https://doi.org/10.1029/2003TC001557.
Plafker, G., 1967, Geologic map of the Gulf of Alaska Tertiary Province, Alaska: U.S. Geological Survey Miscellaneous Geologic Investigations Map 484, https://doi.org/10.3133/i484.
Plafker, G., Hudson, T., and Bruns, T., 1978, Late Quaternary offsets along the Fairweather fault and crustal plate interactions in southern Alaska: Canadian Journal of Earth Sciences, v. 15, p. 805–816, https://doi.org/10.1139/e78-085.
Plafker, G., Moore, J.C., and Winkler, G.R., 1994, Geology of the southern Alaska margin, *in* Plafker, G., and Berg, H.C., eds., The Geology of Alaska: Boulder, Colorado, Geological Society of America,The Geology of North America, v. G-1, p. 389–449, https://doi.org/10.1130/DNAG-GNA-G1.389.
Rau, W.W., Plafker, G., and Winkler, G.R., 1983, Foraminiferal biostratigraphy and correlations in the Gulf of Alaska Tertiary Province: U.S. Geological Survey Oil and Gas Investigation Chart 120, https://doi.org/10.3133/oc120.
Reimer, P.J., Bard, E., Bayliss, A., Beck, J.W., Blackwell, P.G., Bronk Ramsey, C., Buck, C.E., Cheng, H., Edwards, R.L., Friedrich, M., Grootes, P.M., Guilderson, T.P., Haflidason, H., Hajdas, I., Hatté, C., Heaton, T.J., Hoffmann, D.L., Hogg, A.G., Hughen, K.A., Kaiser, K.F., Kromer, B., Manning, S.W., Niu, M., Reimer, R.W., Richards, D.A., Scott, E.M., Southon, J.R., Staff, R.A., Turney, C.S.M., and van der Plicht, J., 2013, IntCal13 and Marine13 radiocarbon age calibration curves 0–50,000 years cal BP: Radiocarbon, v. 55, p. 1869–1887, https://doi.org/10.2458/azu_js_rc.55.16947.
Reitman, N.G., Bennett, S.E.K., Gold, R.D., Briggs, R.W., and DuRoss, C.B., 2015, High resolution trench photomosaics with structure from motion: Workflow and accuracy assessment: Bulletin of the Seismological Society of America, v. 105, no. 5, p. 2354–2366, https://doi.org/10.1785/0120150041.
Risley, D., Martin, G., Lynch, M., Flett, T., Larson, J., and Horowitz, W., 1992, Geologic Report for The Gulf of Alaska Planning Area: U.S. Minerals Management Service Outer Continental Shelf Report MMS 92-0065.
Radbruch-Hall, D.H., Varnes, D.J., and Savage, W.Z., 1976, Gravitational spreading of steep-sided ridges (sackung) in western United States: Bulletin of the International Association of Engineering Geology, v. 13, p. 23–35, https://doi.org/10.1007/BF02634754.
Scharer, K., Weldon, R.I.I., Streig, A., and Fumal, T., 2014, Paleoearthquakes at Frazier Mountain, California delimit extent and frequency of past San Andreas Fault ruptures along 1857 trace: Geophysical Research Letters, v. 41, p. 4527–4534, https://doi.org/10.1002/2014GL060318.
Schell, M.M., and Ruff, L.J., 1989, Rupture of a seismic gap in southeastern Alaska: The 1972 Sitka earthquake (Ms 7.6): Physics of the Earth and Planetary Interiors, v. 54, p. 241–257, https://doi.org/10.1016/0031-9201(89)90246-X.
Stauder, W., 1960, The Alaska earthquake of July 10, 1958: Seismic studies: Bulletin of the Seismological Society of America, v. 50, p. 293–322.
Sykes, L.R., 1971, Aftershock zones of great earthquakes, seismicity gaps, earthquake prediction for Alaska and the Aleutians: Journal of Geophysical Research, v. 76, p. 8021–8041, https://doi.org/10.1029/JB076i032p08021.
Sylvester, A.G., 1988, Strike-slip faults: Geological Society of America Bulletin, v. 100, no. 11, p. 1666–1703, https://doi.org/10.1130/0016-7606(1988)100<1666:SSF>2.3.CO;2.
Teyssier, C., and Tikoff, B., 1998, Strike-slip partitioned transpression of the San Andreas fault system: A lithospheric-scale approach: Geological Society of London, Special Publications, v. 135, no. 1, p. 143–158, https://doi.org/10.1144/GSL.SP.1998.135.01.10.
Tocher, D., 1960, The Alaska earthquake of July 10, 1958: Movement on the Fairweather fault and field investigation of southern epicentral region: Bulletin of the Seismological Society of America, v. 50, p. 267–292.
Tocher, D., and Miller, D.J., 1959, Field observations on effects of Alaska earthquake of 10 July 1958: Science, v. 129, p. 394–395, https://doi.org/10.1126/science.129.3346.394.
U.S. Geological Survey, 2015, LandsatLook Images: Landsat 8 satellite image of Glacier Bay National Park acquired September 22, 2015: U.S. Geological Survey, http://landsat.usgs.gov/LandsatLookImages.php (accessed 3 April 2017).
U.S. Geological Survey, 2016, 5 meter Alaska Digital Elevation Models (DEMs): USGS National Map 3DEP Downloadable Data Collection, http://nationalmap.gov/3DEP/ (accessed 3 April 2017).
Vine, F.J., 1966, Spreading of the ocean floor: New evidence: Science, v. 154, p. 1405–1415, https://doi.org/10.1126/science.154.3755.1405.
Wallace, R.E., 1990, The San Andreas Fault System, California: U.S. Geological Survey Professional Paper 1515, 283 p.
Witter, R., and Bender, A., 2020, Radiocarbon data for Fairweather fault investigation, Glacier Bay National Park, southeast Alaska (2020): U.S. Geological Survey data release, https://doi.org/10.5066/P9Q08JGV.
Witter, R.C., LeWinter, A., Glennie, C., Hauser, D., Bender, A., and Finnegan, D., 2017a, Digital elevation models of Glacier Bay National Park, between Lituya Bay and Icy Point, Alaska, derived from airborne lidar data acquired in September 2015: U.S. Geological Survey data release, https://doi.org/10.5066/F7W094D4.
Witter, R.C., LeWinter, A., Bender, A.M., Glennie, C., and Finnegan, D., 2017b, Sculpted by water, elevated by earthquakes—The coastal landscape of Glacier Bay National Park, Alaska: U.S. Geological Survey General Information Product, v. 177, https://doi.org/10.3133/gip177.
Zielke, O., and Arrowsmith, J.R., 2012, LaDiCaoz and LiDARimager-MATLAB GUIs for LiDAR data handling and lateral displacement measurement: Geosphere, v. 8, p. 206–221, https://doi.org/10.1130/GES00686.1.
Zielke, O., Klinger, Y., and Arrowsmith, J.R., 2015, Fault slip and earthquake recurrence along strike-slip faults—Contributions of high-resolution geomorphic data: Tectonophysics, v. 638, p. 43–62, https://doi.org/10.1016/j.tecto.2014.11.004.